

RESEARCH

Open Access



Modeling of concrete-filled PVC tube columns confined with CFRP strips under uniaxial eccentric compression: machine learning and finite element approaches

Yan Wang¹, Mohamed A. Elmelygy², Haytham F. Isleem^{3,4*} , Asmaa Y. Hamed⁵, Diyar N. Qader⁶, Mohamed Sharaf⁷, Pradeep Jangir⁴, Arpita⁴ and Ghanshyam G. Tejani^{8,9}

*Correspondence:
isleemhaytham88@gmail.com;
mps565@york.ac.uk

¹ School of Mechanical and Electrical Engineering, Guilin University of Electronic Technology, Guilin 541004, China

² Advanced Manufacturing Institute, King Saud University, P.O. Box 800, Riyadh 11421, Saudi Arabia

³ Jadara University Research Center, Jadara University, Irbid, Jordan

⁴ Department of Computer Science, University of York, York YO10 5DD, UK

⁵ Construction and Building Department, The Higher Institute of Engineering and Technology Luxor, Luxor, Egypt

⁶ Civil Engineering Department, University of Kirkuk, Kirkuk, Iraq

⁷ Industrial Engineering Department, College of Engineering, King Saud University, P.O. Box 800, 11421 Riyadh, Saudi Arabia

⁸ Applied Science Research Center, Applied Science Private University, Amman 11931, Jordan

⁹ Department of Industrial Engineering and Management, Yuan Ze University, Taoyuan, Taiwan

Abstract

This paper presents an analytical and finite element modeling (FEM) investigation on the carbon fiber reinforced polymer concrete-filled polyvinyl chloride tube (CCFPT) concrete columns under axial eccentric compression. The study involved collecting experimental data from 32 CCFPT columns confined with CFRP from literature and modeling them using FEM in ABAQUS. A parametric study was conducted on 260 CCFRP concrete columns, examining various parameters such as eccentricity, number of CFRP layers, thickness of PVC tube, column slenderness ratio, CFRP spacing, thickness of CFRP strips, confined concrete strength, and concrete core diameter. The effects of these parameters on the ultimate load and strain capacity were analyzed. Analytical models were developed to express the confined concrete strength and strain as functions of the constituent properties and dimensionless confinement parameters. The findings revealed that increasing eccentricity significantly reduced the ultimate load (up to 45%) and strain (up to 67%) capacities. Adding more layers of CFRP increased strength and strain capacities by 25% when going from 2 to 3 layers at a 20 mm eccentricity. Thicker PVC tubes increased load capacity by preventing buckling, but had inconsistent effects on strain. Higher slenderness ratios decreased both capacities, particularly strain. Six machine learning models were employed to predict the load-carrying capacity and confined ultimate strain. Various performance metrics, data visualization techniques, SHAP analysis, sensitivity analysis, and error characteristic curves were used to evaluate the prediction performance and analyze the impact of input parameters. The findings revealed that increasing eccentricity and CFRP layers lead to reduced ultimate load and strain capacities, while higher slenderness ratios result in increased ultimate loads. The study concluded that CCFPT columns with optimized CFRP wrapping can offer superior performance for eccentrically loaded columns.

Keywords: Carbon fiber reinforced polymer, Finite element modeling, Concrete-filled PVC tubes, Eccentric loading

Introduction

Composite structures, such as concrete-filled steel tubes, but often lack Polyvinyl chloride (PVC) materials are recommended for their mechanical and durable properties. They are cost-effective and perform well over time. Concrete-filled PVC tube (CFPT) columns offer high strength, better durability, and other advantages. Additionally, fiber-reinforced polymer (FRP) materials, such as aramid fiber reinforced polymer (AFRP), carbon fiber reinforced polymer (CFRP), and glass fiber reinforced polymer (GFRP), improve the characteristics of concrete columns [1–5]. They enhance strength, resist corrosion, and are lightweight. Partial wrapping of FRP improves the behavior of composite columns [5–8]. Carbon fiber reinforced polymer (CFRP)-wrapped CFPT (CCFPT) columns are cost-effective, have higher load-carrying capacity, and good durability properties. Several studies [9–14] have thoroughly examined the effect of concentric loading on the behavior of FRP-PVC confined concrete columns. Fakharifar and Chen [9] introduced a unique composite confining system utilizing compressible foam, PVC tube, and an FRP wrap. The FRP-wrapped concrete cylinders exhibited increased strength, while the concrete-filled PVC tube cylinders showed greater ductility. Saafi [10] proposed a PVC-FRP confined concrete column, using a PVC tube in place of the FRP tube and wrapping FRP around the PVC tube. The results demonstrated significant improvements in the bearing and ductility capability of the core concrete, leveraging the combined benefits of PVC, FRP, concrete, and steel. Jiang et al. [12] thoroughly examined the impact of the slenderness ratio on the bearing capacity of long columns under axial compression, revealing that lowering the slenderness ratio improves the bearing capacity. Yu et al. [6] rigorously studied the seismic behavior of PVC-CFRP confined reinforced concrete columns under combined axial compression load and horizontal reversed cyclic loading. The study explored the effects of axial compression ratio and CFRP strip spacing on secant stiffness and energy dissipation. The impact of CFRP strip spacing was especially notable in specimens with higher axial compression ratios, showing a rapid decrease in secant stiffness with increasing axial compression ratio.

In practical applications, it is important to recognize that most concrete columns are subjected to eccentric loading. This factor emphasizes the need for careful consideration and evaluation of the column design to ensure structural integrity. Yu et al. [13, 14] conducted comprehensive experimental studies on PVC-FRP confined concrete columns subjected to both axial and eccentric compression loading. Their investigation analyzed the effects of eccentricity, reinforcement ratio, slenderness ratio, and hoop spacing of FRPs on ductility capacity, failure mode, and bearing capacity. Furthermore, Yu et al. [15–17] carried out comprehensive experimental studies, theoretical analyses, and numerical simulations on PVC-CFRP Confined Concrete Beam-Column Joints (PCCB-CJs) under axial compression. Their findings unequivocally demonstrated the convenience, effectiveness, and feasibility of this connection form for integrating PFCC columns and beams. They also put forward a robust formula for predicting the ultimate bearing capacity and established a precise stress-strain relationship model for the PCCBCJs under axial compression. However, these studies were exclusively focused on FRP-confined reinforced concrete columns with internal steel reinforcement. Limited attention has been given to the behavior of eccentrically loaded FRP-confined PVC-concrete columns without internal steel reinforcement. These studies have revealed distinct behavior

patterns for concrete columns under eccentric compression compared to those under concentric compression, owing to the significant impact of load eccentricity on confinement actions. Nevertheless, they have arrived at conflicting conclusions regarding the effect of load eccentricity on the axial stress–strain behavior of FRP-confined concrete.

Machine learning (ML) algorithms have significantly advanced in recent years due to expanded databases, leading to their widespread use in civil engineering. They play a crucial role in predicting the behavior and strength of structural components, designing fire-resistant structures, and monitoring structural health [18, 19]. In the prediction of the strength of CFST columns, researchers have effectively utilized machine learning techniques [20–26]. Bardhan et al. [27] utilized an ANN with AGWO and a database of 559 test data points to accurately forecast the ultimate load of CFST columns. Additionally, Hou et al. [28] developed multiple ML models based on a database of 2045 test data points, including BPNN, GA, RBFNN, GPR, and MLR, all of which outperformed existing design codes in predicting CFST column strength. Isleem et al. [23, 25, 29–31] conducted an integrated behavioral analysis of FRP-confined circular columns using FEM and ML. They also studied FRP-confined concrete-steel double skin tubular columns under axial compression and modeled tubed reinforced concrete columns under eccentric axial compression loading.

The current paper presents a numerical study that used the FEM to investigate the failure mode, ultimate bearing capacity, and confinement strain of CFRP-PVC-confined concrete columns under eccentric loading. The study considered various parameters, such as confined concrete strength, reinforcement, hoop spacing, column slenderness ratio, PVC tube thickness, and sample sizes, and their impact on the load–displacement characteristics of composite columns. Additionally, the study examined how variables such as CFRP thickness, CFRP hoop spacing, and the number of CFRP layers affect these characteristics. By providing a comprehensive understanding of the behavior of composite columns under eccentric loading, this study aims to contribute to the development of more durable and cost-effective composite structures for diverse applications. Furthermore, six machine learning (ML) techniques were used to predict the effects of changing the structural parameters on the performance of CFRP-PVC confined concrete columns. The techniques used include K-Nearest neighbor (KNN), Linear regression (LR), Bagging regression (BR), XG Boost regression (XBR), Gradient boosting Regression (GBR), and Random Forest (RF). The study aimed to predict two outputs: load-carrying capacity (kN) and confined ultimate strain (mm/mm). However, the prediction for load-carrying capacity (kN) and confined ultimate strain models was not implemented directly in this study. The various ML models were combined with other models based on their individual evaluation and prognosis outputs. The combinations suggested in this study are ETR-BR, GBR-BR, XGB-LR, GBR-LR, BR-LR, and RF-LR, and the models are utilized with optimized hyperparameters. To develop and evaluate the prediction model, the study utilized a dataset of 260 test results gathered through FEM simulations. Reliable regression models were developed and tested in ML using input parameters that impact the predicted value. The study considered eight input parameters, such as slenderness ratio (SR), confinement by PVC material (λ_{PVC}), confinement by internal hoop reinforcement (λ_h), longitudinal reinforcement to the column performance

(λ_l), confinement by CFRP material (λ_{CFRP}), eccentric loading to specimen's diameter ratio (e/D), standard concrete strength (f_{co} (MPa)), and area of concrete core without taking into account the longitudinal steel rebars (A_c (mm^2)), in order to predict two output parameters: load-carrying capacity (P_{cc} (kN)) and confined concrete strain (ε_{cc} (mm/mm)). Figure 1 illustrates the research methodology employed for this study.

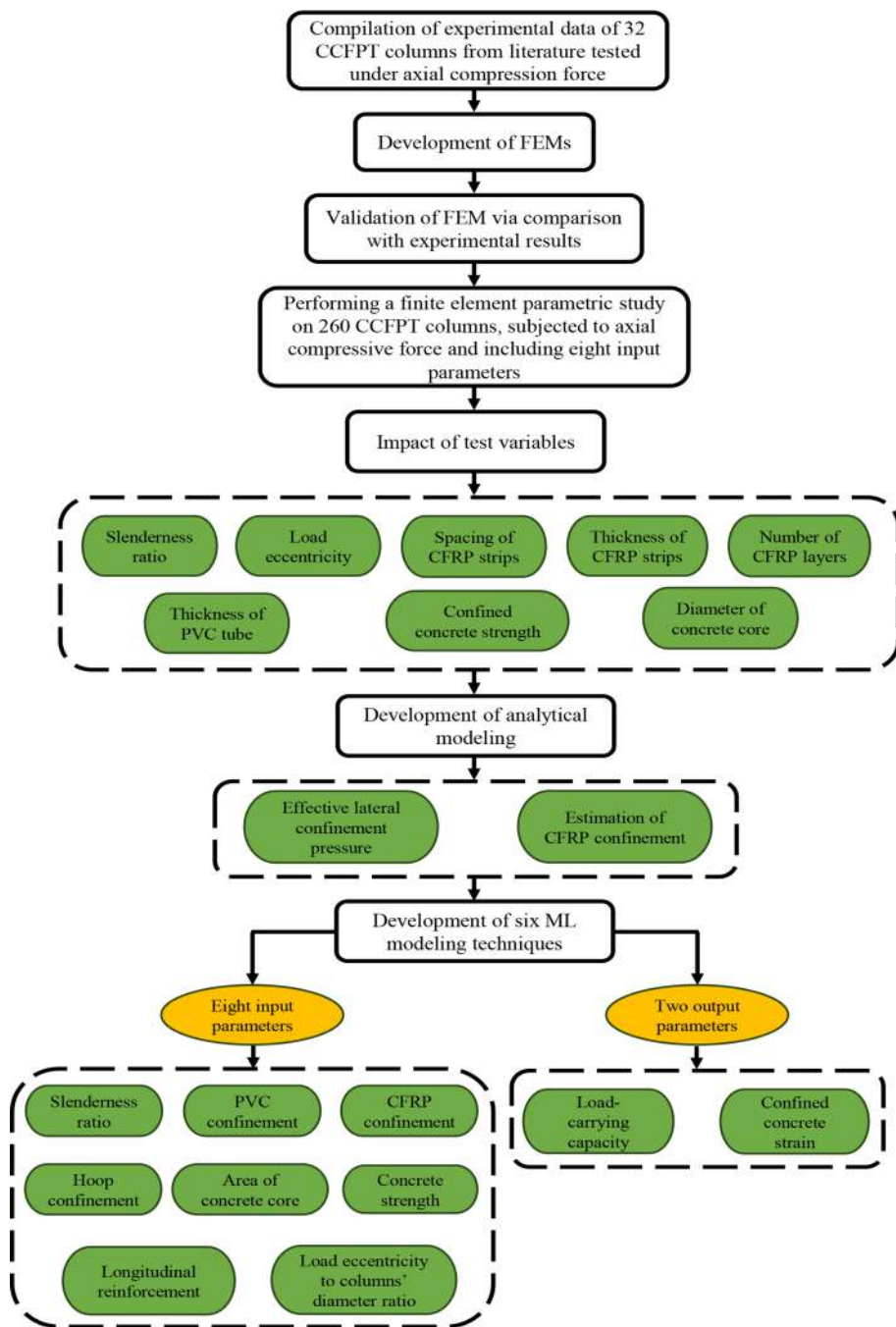


Fig. 1 Flowchart of the research methodology

Summary of database

The main purpose of this research is to develop ML models that accurately predict the axial capacity of circular PVC concrete columns wrapped with CFRP under eccentric loading. To ensure the ML models are well-trained, a large amount of training data is necessary. To achieve this, initially, a database was created, comprising 36 CCFPT concrete columns that underwent experimental testing under axial compressive force. Data for this compilation were sourced from eight studies available in the literature [3, 11, 32–38]. Furthermore, Isleem et al. [39, 40] reported and analyzed confined concrete columns by varying parameters such as specimen size, slenderness ratio, PVC tube thickness, unconfined concrete strength, and steel reinforcement. Secondly, FEM simulation was used to supplement the training set and fill in any gaps in the existing experimental database. The following sections will cover the experimental database and FEM process, including the consideration of various parameters such as eccentric load.

Experimental database

Experimental studies on circular CFRP-PVC confined concrete columns subjected to concentric loading. To address this gap, a comprehensive test database was compiled for this study, consisting of 32 specimens, as illustrated in Table 1. All specimens in the database were subjected to concentric loading. Notably, 13 specimens contain internal steel reinforcement. As indicated in Table 1, the compressive strengths of the concrete ranged from 10.5 to 51.5 MPa. The PVC tubes had tensile strengths ranging from 34.2 to 62 MPa, while the CFRP had tensile strengths between 3612 and 4420 MPa. CFRP thickness of one layer varied from 0.11 to 0.167 mm. The outer diameter of PVC tube ranged from 90 to 200 mm, while the thickness of the PVC tube ranged from 2.55 to 7.8 mm. The height-to-diameter ratio (H/D) ratio for all specimens was between 2.0 and 6.25.

FEM database

The experimental data provided by references [3, 11, 32–38] was supplemented by the FEM database, effectively covering missing information. The selected ranges were determined based on parameters in the experimental data and the material behavior described by the constitutive model used in the FEM modeling. Therefore, Table 2 presents the classification of all specimens, cross-sections, and material details. A total of 260 CCFPT concrete columns were numerically simulated using ABAQUS software [41], and the statistical details of the datasets are reported in Table 2 and Annexure I.

To expand the investigation and to predict two output parameters (load-carrying capacity (P_{cc} (kN)) and ultimate strain (ε_{cc} (mm/mm))), these 260 simulated CCFPT concrete columns are collected for further studies using six modern ML techniques with eight input parameters such as slenderness ratio (SR), confinement by PVC material (λ_{PVC}), confinement by internal hoop reinforcement (λ_h), longitudinal reinforcement to the column performance (λ_l), confinement by CFRP material (λ_{CFRP}), eccentric loading ratio (e/D), standard concrete strength (f_o (MPa)), and area of concrete core without taking into account the longitudinal steel rebars (A_c (mm²)).

Table 1 Experimental database of CFRP-PVC confined concrete columns collected from Ref [3, 11, 32–37]

Refs.	No	Geometric properties				Internal steel reinforcement				Material properties			
		CFRP		PVC and concrete core		longitudinal steel bars		Hope steel bars		PVC		CFRP	
		n_f	t_f -one layer (mm)	C_f (mm)	t_p (mm)	D (mm)	H/D	D_c (mm)	D_t (mm)	f_{pvc} (MPa)	f_{fr} (MPa)	f_{co} (MPa)	
Feng and Daitao [11]	1	3	0.111	20	7.8	200	500	2.5	184.4	8 φ10mm	6 mm@104 mm	62	3612 29.8
Fang et al. [32]	1	3	0.111	20	7.8	200	500	2.5	184.4	0	0	62	3612 28.5
Chang et al. [33]	1	3	0.165	20	5.0	168	588	3.5	158.0	0	0	61.73	3612 29.0
Guo et al. [3]	1	3	0.167	20	4.0	165	495	3	157.0	0	0	50	4420 26.88
Bandyopadhyay et al. [34]	12	0	0	0	2.55-5.8	160	500-1000	3.125-6.25	149.2-155.4	10 φ10mm	6 mm@104 mm	39.79	0 28.3-33.1
Woldemariam et al. [35]	12	0	0	0	3	90-110	180-280	2-3.11	84-134	0	0	49.72	0 10.5-24.1
Alatshani et al. [36]	2	0	0	0	3	100-150	225-338	2.25-3.38	94-144	0	0	34.2	0 15.0-35
Gupta et al. [37]	2	0	0	0	3.9-4.3	140-160	500	3.57-3.12	132.2-151.5	0	0	52	0 30-51.5
Max	32	3	0.167	20	7.8	200	1000	6.25	184.4			62	4420 51.5
Min	0	0	0	0	2.55	90	255	2.0	84			34.2	0 10.5

n_f number of layers CFRP; C_f (mm) center to center spacing of CFRP for partial wrapping, t_f -one layer(mm) thickness of one-layer CFRP, D , t_p (mm) diameter and thickness of PVC tube, H (mm) height of column, D_c (mm) diameter of concrete core, f_{pvc} (MPa) = tensile strength of PVC tube, f_{fr} (MPa) tensile strength of CFRP sheets, and f_{co} (MPa) compressive strength of concrete core

Table 2 Description of FEM database based on experimental database in Ref [3, 11, 32–37]

Ref.	No	Geometric properties			PVC and concrete core			Eccentric parameter			Material properties			
		CFRP		t_f (mm)	C_f (mm)	D (mm)	H (mm)	H/D	D_c (mm)	ϵ (mm)	f_{PVC} (MPa)	f_{CFRP}	f_{tr} (MPa)	f_{co} (MPa)
		n_f	t_f -one layer (mm)											
Group 1	39	3	0.165	20	2.55–7.8	90–200	255–1000	2.0–6.25	84–184.4	20	34.2–62	3612	10.5–51.5	
Group 2	39	3	0.165	20	2.55–7.8	90–200	255–1000	2.0–6.25	84–184.4	30	34.2–62	3612	10.5–51.5	
Group 3	37	3	0.165	20	2.55–7.8	90–200	255–1000	2.0–6.25	84–184.4	40	34.2–62	3612	10.5–51.5	
Group 4	39	3	0.165	20	2.55–7.8	90–200	255–1000	2.0–6.25	84–184.4	0	34.2–62	3612	10.5–51.5	
Group 5	39	1	0.165	20	2.55–7.8	90–200	255–1000	2.0–6.25	84–184.4	0	34.2–62	3612	10.5–51.5	
Group 6	39	2	0.165	20	3	90–110	180–280	2–3.11	84–134	20	34.2–62	3612	10.5–51.5	
Group 7	28	1,2,3	0.165	20	7.8	200	500	2.5	184.4	30, 40, 50, 60	62	3612	29.8	
Max	260	3	0.165	20	7.8	200	1000	6.25	184.4	60	62	3612	51.5	
Min	1	0.165	0	2.55	90	255	20	84	0	34.2	3612	10.5		

 e (mm) eccentric distance

FEM modeling

Basic simulation conditions

Finite element analysis (FEM) simulations were conducted in this study using ABAQUS [41]. The concrete core, steel end plates, and steel reinforcement were modeled using 8-node linear brick elements with reduced integration (C3D8R) and a truss element T3D2. On the other hand, the 4-node shell elements (S4R) were utilized to simulate the outer CFRP jacket and PVC tube as Ref [39, 42–45], as illustrated in Fig. 2. The interaction between the end loading steel plates, concrete core, and PVC tube was modeled using perfect bonding through the surface-to-surface contact method [31, 46]. Eccentric loading was applied using the displacement control method [39, 43, 46]. Similarly, perfect connection between the CFRP strip and the PVC tube was considered (i.e., no slips), and this was achieved by using the "tie" constraint option available in the ABAQUS software. The master surface for the tie constraint was considered for the CFRP strip, and the slave surface for the tie constraint was considered for the PVC [44, 46]. To accurately represent the end conditions of the columns, as shown in Fig. 2, the bottom loading plate is fully fixed and all displacements and rotations are restricted (i.e. $U_x = U_y = U_z = U_{Rx} = U_{Ry} = U_{Rz} = 0$, where U_x , U_y and U_z are translations in the X, Y and Z directions respectively, and U_{Rx} , U_{Ry} and U_{Rz} are the rotational degrees of freedom about the X, Y and Z axes, respectively). on the other hand, at the top loading plate, all degrees of freedom are again restrained except for U_z , which represents axial displacements in the Z direction. Two reference points (RP1, RP2) were established at the midpoint of each endplate, and the axial displacement was introduced through the upper reference point (RP1) in a concentric manner under displacement control. In order to ensure uniform compression, a reference point

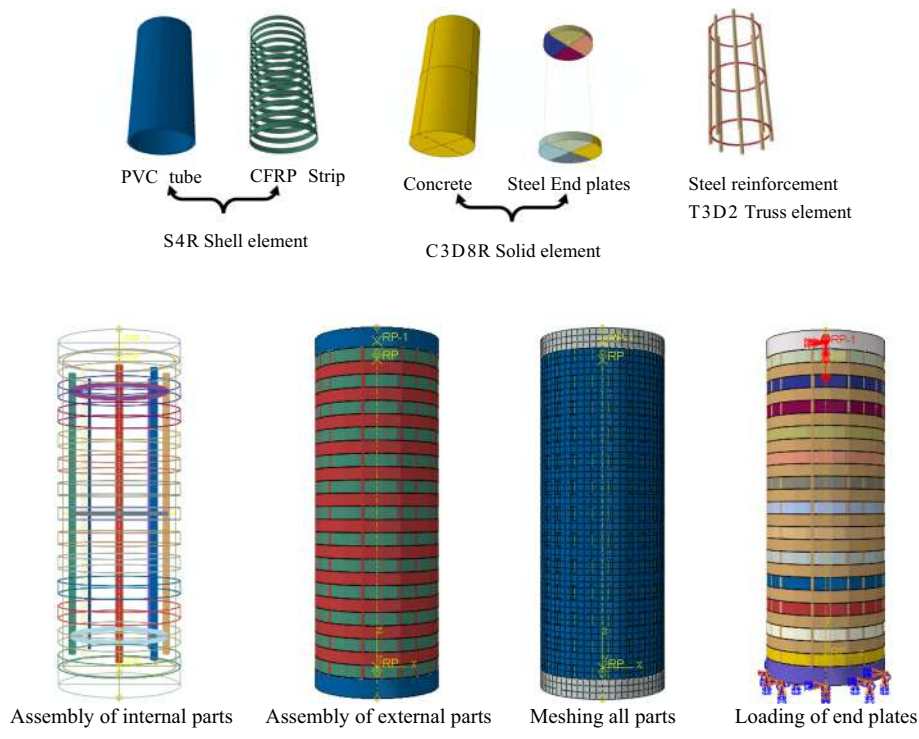


Fig. 2 Basic simulation conditions of element type, boundary condition, and loading of end plates

(RP1) is connected to the upper surface of the top loading end plate, and the axial displacement force is applied to the RP along the Z-axis direction. As a result, the ultimate load (P) responses to the displacement of the specimens were assessed at the reference point. In order to obtain accurate outcomes in a reasonable amount of time, a study was carried out to determine the most suitable mesh size by conducting a mesh convergence analysis. For the concrete core, elements measuring 10 mm have been employed utilizing the Sweep technique. In contrast, elements of 15 mm and 20 mm have been utilized for PVC pipes in columns, both with and without gaps at their respective ends [24, 29, 47–49].

Material modeling

The finite element modeling of the CCFPT column components such as concrete material, steel material, PVC tube, CFRP strip is presented in the following subsections.

Concrete core modeling Since the concrete core is confined by the PVC tube, the model appropriately depicts it as confined concrete. The concrete progresses from the elastic to the plastic stage when it is loaded, which eventually causes failure. The concrete's constitutive model in the elastic area is determined by its elastic modulus (E_c) and Poisson's ratio (ν). According to reference [50], a Poisson's ratio of 0.2 is commonly utilized for concrete. As suggested by [51], the concrete's elastic modulus is obtained from Eq. (1).

$$E_c = 4700\sqrt{f'_c} \quad (1)$$

Here f'_c is the strength of unconfined concrete cylinder under compression (MPa).

When concrete reaches the elastic limit, it starts to move into the plastic zone, which is when the concrete and PVC tubes start to interact. At this point, the concrete's plastic expansion is responsible for the interactions and contact pressure that exist between the PVC tube's inner and outer surfaces. Using techniques from [42, 52, 53], the Concrete Damage Plasticity Model (CDPM) in ABAQUS was used to simulate the concrete core. This analysis took into account five essential variables, which are specified in [39, 40]: the yielding surface shape factor (K_c), viscosity parameter (μ), plastic flow potential eccentricity (e), dilation angle (Ψ), and the ratio of biaxial stress to uniaxial stress of concrete (f_{bo}/f'_c). Nonetheless, the confinement factor $\xi_c = \frac{f_{PVC}A_{PVC}}{f'_c A_c}$ determined the extent to which the PVC tube confined the concrete core. Table 3 provides the particular parameters and Fig. 3a shows the stress-strain characteristics for the concrete used in this study.

At the beginning of loading, the impact of the PVC tube constraint on the concrete core was not taken into consideration. As a result, the concrete core's stress condition is similar to that of unconfined concrete. In order to depict the rising stress-strain response curve up to the peak stress, Eq. (2) [54] was utilized. Equation (3) [39] can be used to calculate the strain of the confined concrete at the first peak load

Table 3 The input parameters of CDPM model, based on Ref [39, 40, 52, 53]

Ψ	K_c	e	f_{bo}/f'_c	μ
35	0.667	0.1	1.16	0.0002

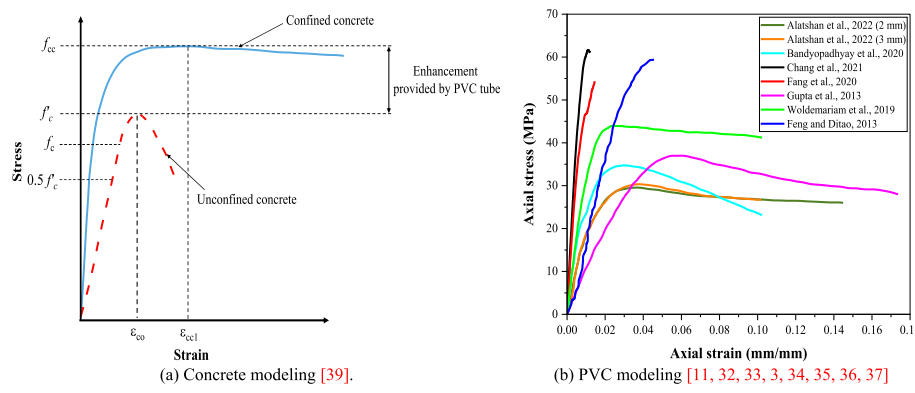


Fig. 3 Stress-strain response for: **a** concrete modelling [39]; **b** PVC modelling [11, 32–37]

(ε_{cc1}). For both confined and unconfined concrete, the elastic stress response in this numerical simulation is 45–50% of the maximum strength of concrete cylinders.

$$\sigma_c = \frac{2f'_c \left(\frac{\varepsilon_c}{\varepsilon_{cc1}} \right)}{1 + \left(\frac{\varepsilon_c}{\varepsilon_{cc1}} \right)^2} \quad (2)$$

$$\left[\frac{\varepsilon_{cc1}}{\varepsilon_c} \right] = 0.808 \left[\frac{H}{D} \right]^{0.5} \left\{ 1 + 6.241 \left[\frac{f_{ls}}{f'_c} \right]^{0.85} + 15.223 \left[\frac{f_{PVC}}{f'_c} \right]^{0.99} \right\} \quad (3)$$

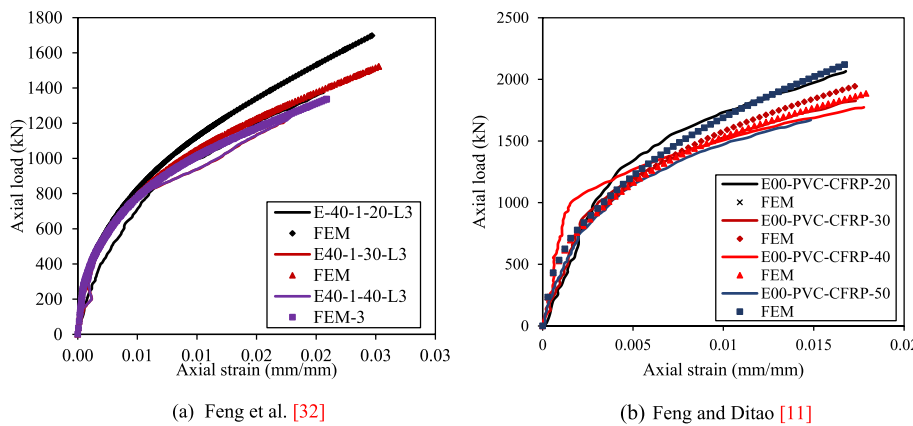
The stress–strain response curve became plateaued at reaching the peak stress, indicating the start of the plastic response stage. The PVC tube provided resistance to the lateral expansion of the concrete core, which resulted in the persistence of this plateau. Using a multi-linear regression analysis, the model proposed by Isleem et al. [40] was used to characterize the strain of the confined concrete core.

Reinforced steel modeling The reinforced steel bars and end loading plate are assumed to follow an ideal elastic-perfectly plastic stress–strain model. The curve is linear in the elastic region and clearly exhibits a distinct yield point. Following the yield strain, the plastic flow initiates, where, modulus of elasticity of 2×10^5 MPa, Poisson's ratio of 0.3, yield stress of 313 and 500 MPa, and fractional external tolerance of 0.05.

PVC tube The axial compression test conducted on the PVC tube allowed for the fitting of its constitutive relation based on the obtained test data [3, 11, 32–37]. PVC tube is regarded as an isotropic material because of its consistent characteristics in all directions and its ductile features with substantial strain capacity. The PVC tube is represented as an iso-tropically hardened von Mises material. Figure 3b shows the stress–strain responses of the PVC tubes that are the subject of this investigation. The PVC material has modulus of elasticity, Poisson's ratio, and ultimate strength, ranging from 2.04 to 4.83 GPa, 0.34 to 0.40, and 27.5 to 68.0 MPa, respectively.

Table 4 The characteristics of CFRP strips utilized in this study [39, 44]

Young's modulus (MPa)			Poisson's ratio			Shear modulus (MPa)		
E_{12}	E_{13}	E_{23}	μ_{12}	μ_{13}	μ_{23}	G_{12}	G_{13}	G_{23}
224000	18581	18581	0.2	0.2	0.3	12576	12576	7147

**Fig. 4** Verification models experimental versus FEM results

CFRP strip In this study, LAMINA material type reported in [39] was utilized to define the properties of CFRP. For this analytical investigation, a tensile failure stress of 3613 MPa and a corresponding tensile failure strain of 0.016122 were selected, agreeing with [44]. The bulk density of CFRP strip used in this study was 1.7×10^{-9} kg/m³, and each layer has a width of 20 mm. The properties of CFRP used in this study are tabulated in Table 4.

Verification of FEM

The comparison of the experimental data and numerical results demonstrates the accuracy and precision of the FEM for validation. Figure 4a, b shows the comparison of the test results and numerical simulations for Feng et al. [32] and Feng and Dita [11]. For further verification of the previous analysis conducted by Isleem et al. [39, 43], the failure modes predicted by the Finite Element Method (FEM), and the corresponding experimental results for a selection of columns were examined. These columns represent a comprehensive range of observed failure modes. The FEMs were successful in capturing the key failure modes observed in the tests, such as the buckling of both the concrete core and the outer PVC tubes. The findings and comparisons presented in this study demonstrate that the FEM analysis accurately depicts the actual response of FRP-wrapped elliptical CFST short columns, including the axial load versus axial displacement responses (see Fig. 5), and the failure modes in reference [39, 43].

Results and discussion

Hoop spacing and confinement stress ratio

The relationship between axial strain and axial load was analyzed using numerical simulations and experimental data. Figure 5a illustrates the impact of different CFRP hoop spacings and zero eccentricity of axial force on these relationships. The curves show that

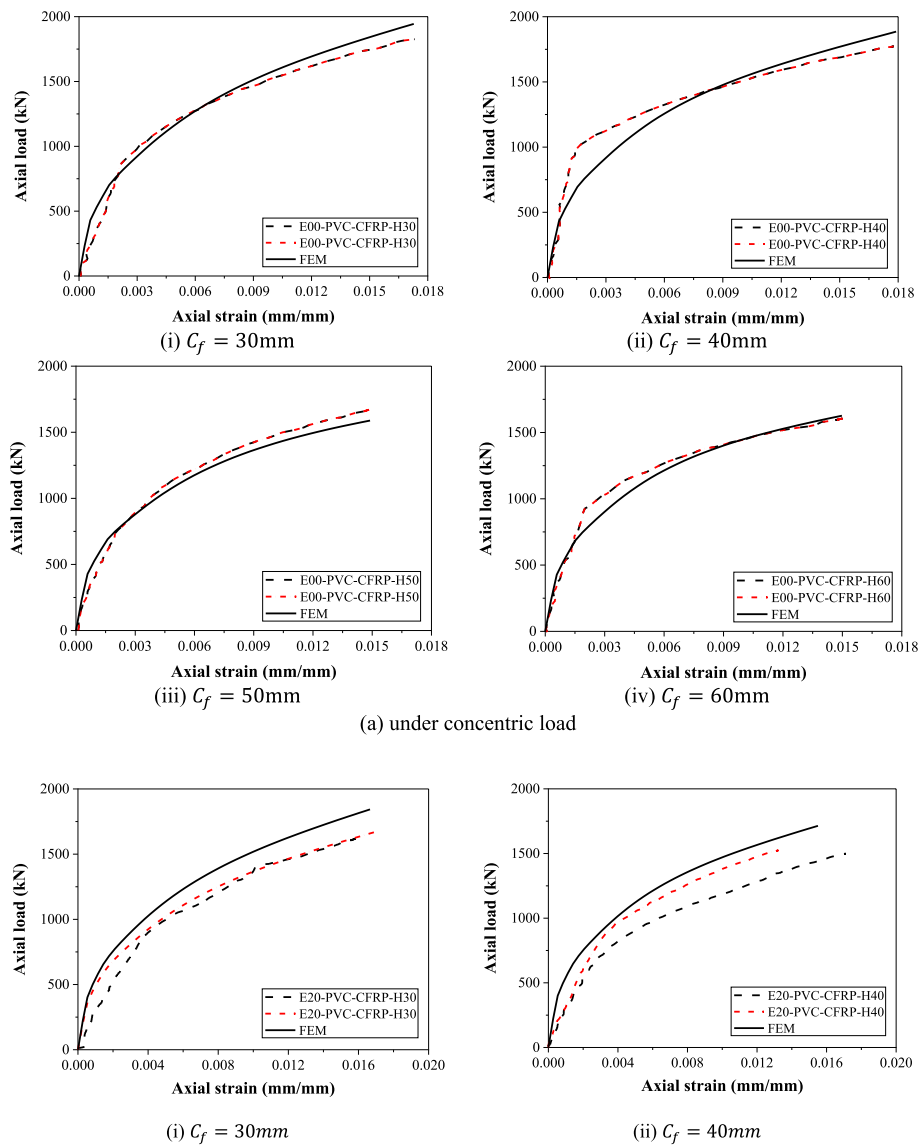
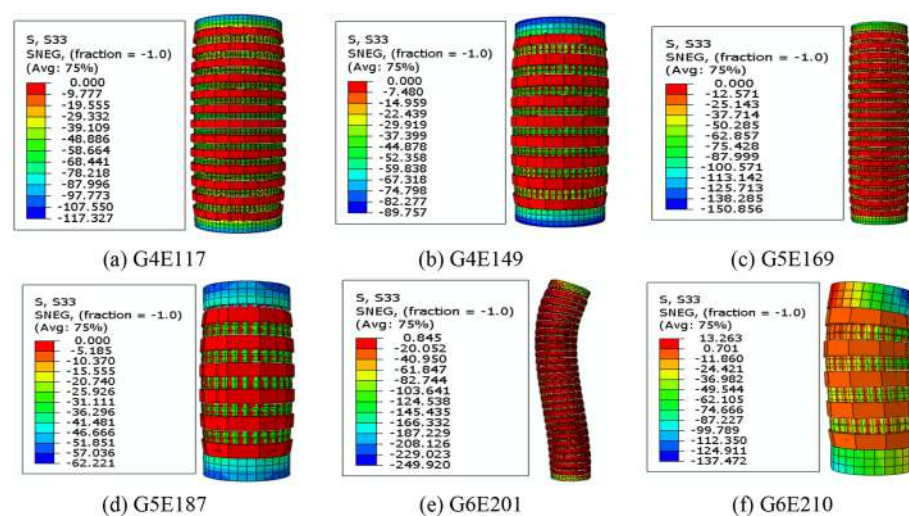
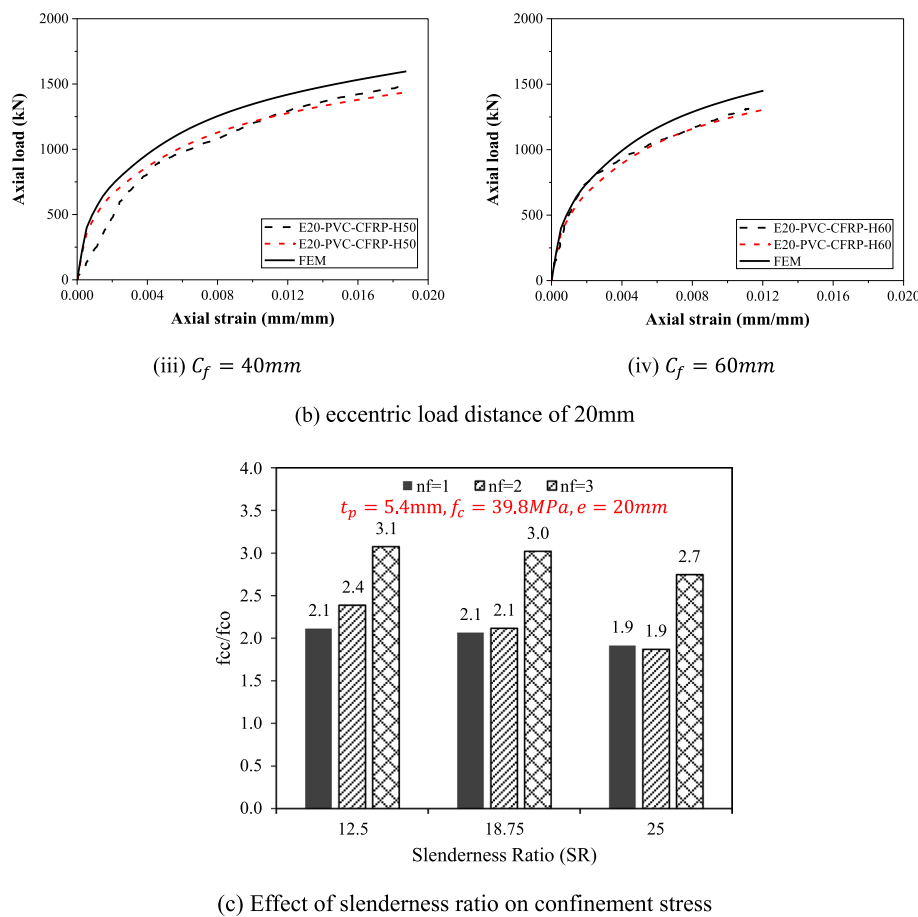


Fig. 5 Effect CFRP hoop spacing and slenderness ratio in axial load-strain and confinement stress

as the CFRP hoop spacing decreases, the load-carrying capacity of the CCFPT specimens also decreases. Additionally, Fig. 5b demonstrates similar trends in load-carrying capacities with varying CFRP hoop spacing. Additionally, in Fig. 5c, the impact of the slenderness ratio on the confinement stress ratio (f_{cc}/f_{co}) regarding the increase in CFRP layers is examined. The results show that as the thickness of CFRP (number of layers) increases, the confinement stress ratio also increases under eccentric load, even as the slenderness ratio increases. However, an increase in the slenderness ratio leads to a decrease in the confinement stress ratio.

Failure mode

The simulated results presented in Fig. 6 illustrate the ultimate load values for the various CCFPT columns listed in Annexure I. As the eccentricity of the CCFPT columns



increased, the ultimate strain in the transverse direction and the ultimate longitudinal strain at the edge of the compressive side also increased. This phenomenon led to the CFRP rupture at that specific position [55].

Parametric analysis

A detailed set of studies was carried out on PVC concrete columns confined with CFRP to thoroughly analyze their performance and evaluate the varying impact of different factors on their overall behavior. Previous research by Isleem et al. [39, 43] suggested that the number of CFRP layers, slenderness ratio of the column, CFRP spacing distance, and total thickness of FRP have the greatest influence on the behavior of CFRP-confined PVC confined concrete columns in terms of ultimate axial stress and ultimate axial strain when loaded with a concentrated load. The parametric analysis involved examining how changing the value of a specific parameter affected the overall axial capacity of the columns when loaded under eccentric load, while keeping all other parameters constant. The parameters studied included:

Eccentric load distance, number of CFRP layers, thickness of PVC tube, slenderness ratio of the column, CFRP spacing distance, confined concrete strength, and diameter of concrete core, on the enhancements of axial load and axial strain in a comprehensive set of 260 simulated CCFPT specimens.

Effect of eccentric distance

In Fig. 7, the effect of different eccentric loading distances on the ultimate load and ultimate strain of CFRP confined PVC concrete columns are shown in Fig. 7. These columns are composed of three layers of CFRP strips and are arranged into groups 1, 2, and 3. As eccentricity increases, there is a decrease in ultimate load and strain. For example, when eccentricity increased from 0 to 20 mm, the ultimate load and strain decreased by an average of 15% and 17% respectively. This trend continued as eccentricity increased further. At eccentricities of 30 and 40 mm, the ultimate loads experienced an average reduction of 40% and 45% respectively, while the ultimate strains experienced an average reduction of 65% and 67% respectively. These findings indicate a simultaneous decrease in confinement efficiency as load eccentricity increases.

Effect of number of CFRP layers

In Fig. 8 the impact of CFRP layers on the ultimate load of CCFPT specimens, particularly in groups 1 and 6, is illustrated. For example, increasing the number of CFRP layers

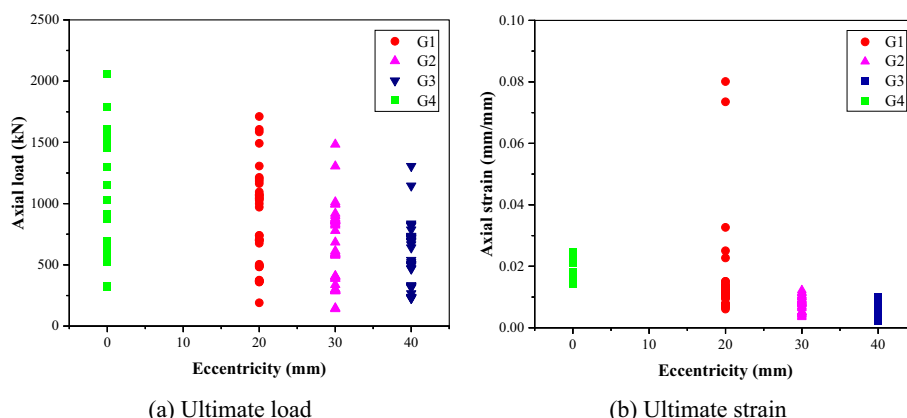


Fig. 7 Effect of different eccentric loading distances

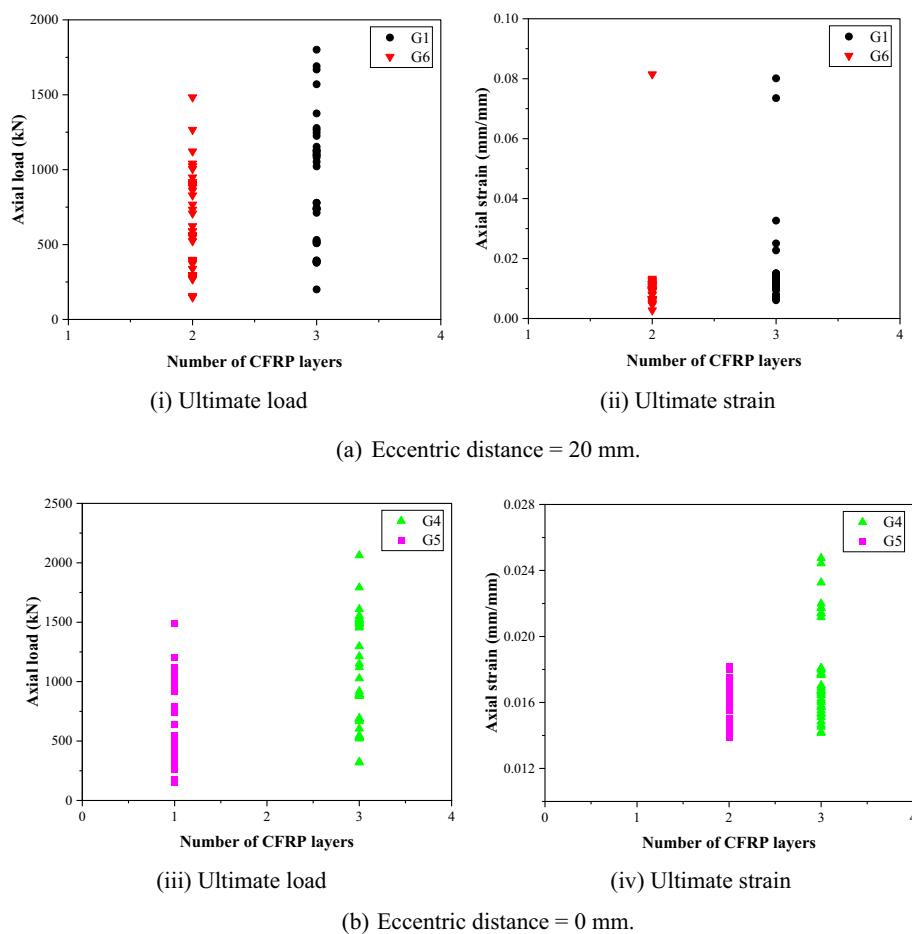


Fig. 8 Effect of number of layers of CFRP on eccentric load

from 2 to 3 results in an average 25% increase in ultimate load for the CCFPT specimen with a 20 mm eccentricity. Similarly, as shown in Fig. 8b, increasing the number of layers from one to three led to an average increase in ultimate load of around 64% for specimens with an eccentricity of 0 mm. Additionally, Fig. 8b demonstrates that the inclusion of a third layer resulted in an average increase in ultimate strain of almost 9% for the CCFPT specimen with an eccentricity of 0 mm.

After analyzing the experimental and FEM results, it was found that increasing the number of CFRP layers in CCFPT specimens led to a higher ultimate load-carrying capacity at a constant eccentricity distance. Additionally, the ultimate strain showed a proportional rise with the number of CFRP layers as the eccentricity distance increased [56].

Effect of PVC tube thickness

The influence of PVC tube thickness on the ultimate load and ultimate strain of CCFPT columns at different eccentric load distances is shown in Fig. 9. Increasing PVC tube thicknesses enhances load-carrying capabilities for certain eccentricities. Specifically, at a PVC thickness was 2.3 mm, the ultimate load-carrying capacity improved by 44.95%, 50.84%, and 53.55% for slenderness ratios of 18 and 25, respectively. Similarly, substantial

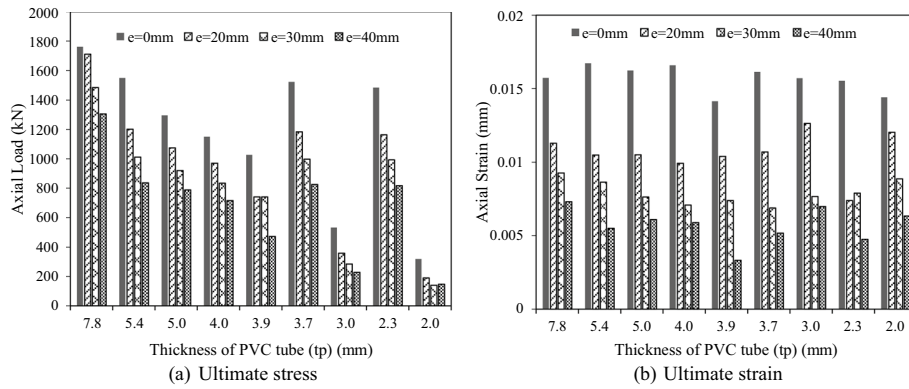


Fig. 9 Effect of PVC thickness on **a** Ultimate stress, **b** Ultimate strain

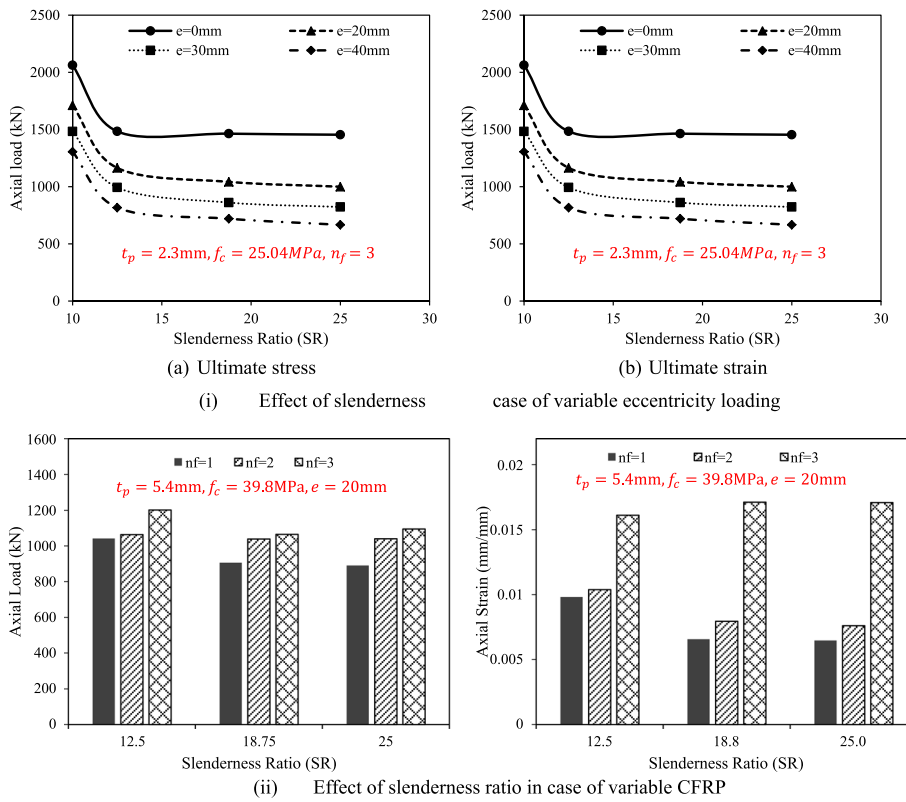


Fig. 10 Effect of slenderness ratio (SR) on **a** Ultimate stress, **b** Ultimate strain

gains in ultimate load-carrying 45.81% and 46.00% were noted at a slenderness ratio of 12.5 for PVC thicknesses of 3.7 mm and 5.4 mm.

Effect of column's slenderness ratio

Figure 10i shows the impact of slenderness ratio on the axial load and strain of CCFPT columns, which have three CFRP layers and a 2.3 mm PVC tube. As the load eccentricity distance increases, there is a notable reduction in ultimate load and strain, with larger drops observed for higher slenderness ratios. Larger diameter specimens are more prone

to crushing, while smaller diameters are more susceptible to buckling [57–59]. Overall, the decrease in ultimate strain is more significant than the reduction in ultimate load capacity, regardless of slenderness ratio. Furthermore, in Fig. 10ii, CFRP confinement is more important at higher slenderness ratios. While CFRP layers enhance ductility and strength, their effectiveness may decrease at very high slenderness ratios, where global buckling becomes the main failure mode. The ultimate strain in axially loaded specimens increases with the number of CFRP layers. Additionally, an increase in the number of CFRP layers improves load-carrying capacity across various slenderness ratios.

Impact of CFRP spacing

The impact of eccentric loading distances and CFRP clear spacing on the ultimate load and ultimate strain of CCFPT concrete columns is shown in Fig. 11. The load bearing capacity of CCFPT specimens decreased with an increase in the clear spacing between CFRP layers, as shown in Fig. 11a. This effect was most pronounced for specimens with three CFRP layers, regardless of the load eccentricity distance. Moreover, for both 20- and 40-mm eccentricities, Fig. 11b indicates a decrease in the specimens' ultimate strain carrying capacity as the clear spacing between CFRP layers increases. An increase in CFRP layers has been shown to boost the axial load-carrying capacity and axial strain carrying capacity of composite columns in earlier research [9]. Furthermore, the presence of CFRP has a major impact on the stress-strain behavior of concrete specimens with external CFRP wrapping. When the strength of CCFPT samples approaches a maximum, observations also show enhanced cracking in the interfacial transition zone and rapid fiber cracking [60].

Impact of confined concrete strength

The influence of concrete strength on the axial load/strain characteristics of CCFPT columns with three layers of CFRP strips and different eccentric load distance is shown in Fig. 12. In Fig. 12a illustrates that, regardless of the concrete strength, the ultimate load-carrying capacity decreased as the eccentric load distance increased from 0 to 40 mm. Furthermore, the ultimate load decreased as concrete strength increased between 10.5 and 15.0 MPa, independent of the eccentric load distance. Significantly, the maximum load-carrying capacity increased over 15.0 MPa concrete

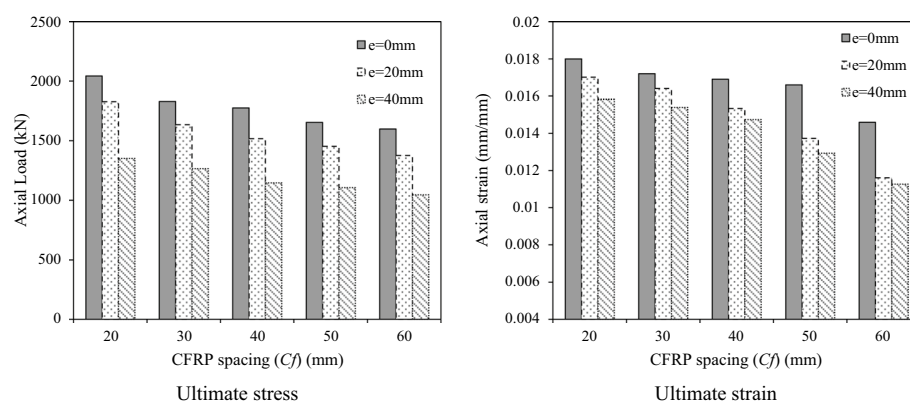


Fig. 11 Effect of CFRP spacing (C_f) on **a** Ultimate stress, **b** Ultimate strain

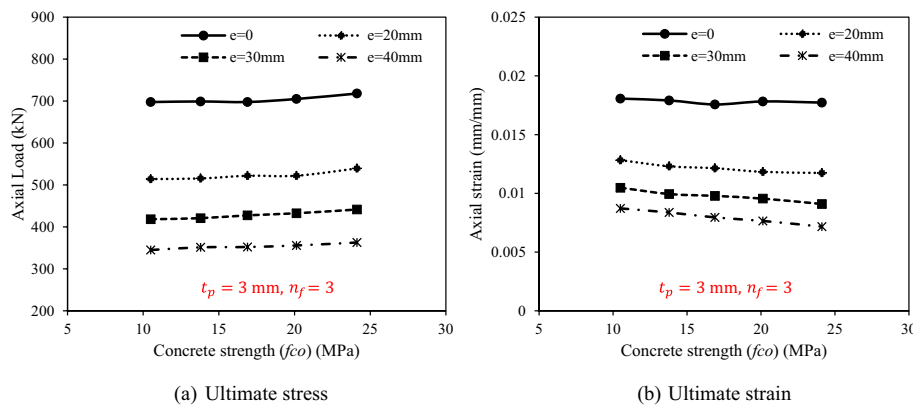


Fig. 12 Effect of concrete strength (f_{co}) (MPa) on **a** Ultimate stress, **b** Ultimate strain

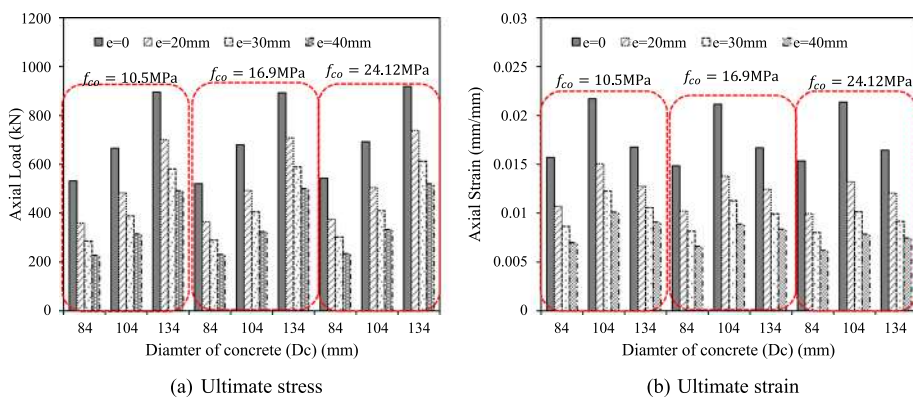


Fig. 13 Effect of diameter of concrete core (D_c) (mm) on **a** Ultimate stress, **b** Ultimate strain

strength; the rate of increase was greater for higher concrete strengths. Figure 12b shows that, although at a somewhat slow rate of reduction, the increase in concrete strength resulted in a decrease in ultimate strain up to a concrete strength of 15.0 MPa. But as the concrete strength increased over this point, the ultimate strain reduction rate became more significant.

Impact of the diameter of concrete core

Figure 13 shows the effect of the concrete core's diameter on the axial load and strain of CCFPT columns that have three layers of CFRP strips with different eccentric load distances. The findings show that as the eccentrically loaded distance increases from 0 to 40 mm, there is a noticeable decrease in both ultimate load and ultimate strain. Additionally, a decrease in the concrete core's diameter is found to be correlated with a decrease in both ultimate load and strain. Figure 13a demonstrates that the ultimate load reduction rate is relatively lower for specimens with smaller core concrete diameters and higher for those with larger core concrete diameters. On the other hand, Fig. 13b shows that there is no consistent relationship between ultimate strain and the diameter of the concrete core.

Analytical modeling

Analytical relationships have been developed to express the confined concrete strength of CCFPT columns as a function of the constituent properties, namely, concrete strength and CFRP properties. In addition, these relationships have been utilized to calculate the load-carrying capacity of the columns, while considering other significant parameters that may influence the results.

Effective lateral confinement pressure

It was discovered in the earlier research studies that the use of CFRP, PVC, and longitudinal and hoop reinforcement bars during experimental or simulation tests affected the failure stress and strain [39, 40]. In order to determine the failure stress, a model must be developed with the previously given parameters, depending on the previously mentioned dimensionless parameters [61]. The failure strain of CFRP strip is associated with the rupture strain, and it is calculated by $\varepsilon_{fe} = k_e \varepsilon_{fu}$, whereas ε_{fu} is the ultimate tensile strain of CFRP, and k_e is taken as 0.80. The following dimensionless parameters illustrated in Eqs. (4) to (7) are introduced: PVC tube (λ_{PVC}), longitudinal reinforcement (λ_l), hoop reinforcement (λ_h), and CFRP reinforcement (λ_{CFRP}).

$$\lambda_{PVC} = \frac{\rho_{PVC} f_{PVC}}{f_{co}} \quad (4)$$

$$\lambda_l = \frac{\rho_{ls} f_{yl}}{f_{co}} \quad (5)$$

$$\lambda_h = \frac{\rho_{hs} f_{yh}}{f_{co}} \quad (6)$$

$$\lambda_{CFRP} = \left(\frac{\rho_{CFRP} E_{CFRP}}{2} \right) \varepsilon_{CFRP,R} \quad (7)$$

$$\rho_{PVC} = \frac{4t}{D}$$

$$\rho_l = \frac{\text{Number of bars} \times \text{Rebar area}}{\text{Gross sectional area}}$$

$$\rho_h = \frac{4 \times \text{Hoop rebar area}}{\text{Spacing} \times (D_c - 2 \times \text{Cover})}$$

Here, ρ_{PVC} is a volumetric ratio of PVC tube, ρ_l is a volumetric ratio of longitudinal reinforcement, ρ_h is a volumetric ratio of hoop reinforcement, ρ_{CFRP} is a volumetric ratio of CFRP, f_{yl} is a yield strength of longitudinal reinforcement (MPa), f_{yh} is a yield strength of hoop reinforcement (MPa), ρ_{PVC} is a yield strength of PVC tube (MPa),

E_{CFRP} is a Young's modulus of CFRP (MPa), t is a thickness of PVC tube (mm), and D is a diameter of column specimen (mm).

When the CCFPT columns are fully wrapped, the volumetric ratio is estimated as $\rho_{CFRP} = \frac{4t_{wrap}}{D}$, where, t_{wrap} is the thickness of CFRP layer (mm), and D is the diameter of the specimen section (mm). If the CCFPT columns are partially wrapped, the volumetric ratio is calculated by $\rho_{CFRP} = \frac{4W \times t_{wrap}}{S \times D}$, where S is the spacing between CFRP strips and W is the width of the CFRP strip.

Confinement ratio

An analytical model is developed using MINITAB to examine the impacts of different dimensionless parameters on the confinement offered by the CFRP strips. This model is developed based on two key parameters, namely the specimen's ultimate stress and ultimate strain. The ultimate stress is denoted by f_{cc} while the ultimate strain of CFRP rupture failure is represented by ε_{cc} . The confinement ratio is defined as the ratio between the strength provided by the unconfined concrete to confined concrete. The strength provided by confined concrete is influenced by several factors, as discussed earlier. Existing literature suggests that the influencing parameters and confinement ratio follow an experimentally verified linear relationship [62] and simulation tests [39, 40]. The failure stress expressions were derived using MINITAB by considering two dimensionless parameters and the eccentricity-to-diameter ratio.

$$\frac{f_{cc}}{f_{co}} = 0.3553 + 2.373 \left[\left(\lambda_{PVC}^{0.5} \right) \left(1 + \frac{e}{D} \right)^{-2.1} \right] + 0.3191 \left[\left(\lambda_{CFRP}^{1.5} \right) \left(1 + \frac{e}{D} \right)^{-3} \right] + 1.839 \lambda_h^{0.8} \quad (8)$$

Equation (8) shows the influence of the dimensionless parameters and the ratio of eccentric distance to core diameter specimen on the confinement ratio. Equation (9) represents the expressions for failure strain, which are dependent on the two significant dimensionless parameters and the ratio of eccentricity to diameter. These equations were developed using MINITAB, and the obtained R^2 values were 0.98 and 0.68, respectively.

$$\frac{\varepsilon_{cc}}{\varepsilon_{co}} = \left[1.842 + \left[6.585 \left(\lambda_{PVC}^{0.12} \right) + 0.552 \left(\lambda_{CFRP}^{0.9} \right) \right] \right] \left(1 + \frac{e}{D} \right)^{-5} \quad (9)$$

Estimation of CFRP confinement for sufficiently confined concrete

The influence of three dimensionless parameters on the effectiveness of CFRP confinement is well established [39]. A grouping based on the distribution of non-dimensionless parameters identified two distinct ranges. The first group had a confined ratio ranging from 0.680 to 4.273, λ_{CFRP} ranging from 0.139 to 7.568, λ_{PVC} ranging from 0.079 to 0.632, λ_h ranging from 0 to 0.188, and eccentricity to diameter ratio ranging from 1 to 1.444. Based on a multi-parameter regression analysis of a test database consisting of 146 specimens, Eqs. (10) and (11) were formulated, as illustrated in Fig. 14. These equations can be used to assess the effectiveness of CFRP confinement in circular CCFPT columns, with a correlation coefficient of 93.66%. Furthermore, the proposed relationship defines a modified confined ratio (MCR) of less than 0.70 as lightly confined, based on the results of 146 tests. It is, therefore, recommended not to exceed this limit during

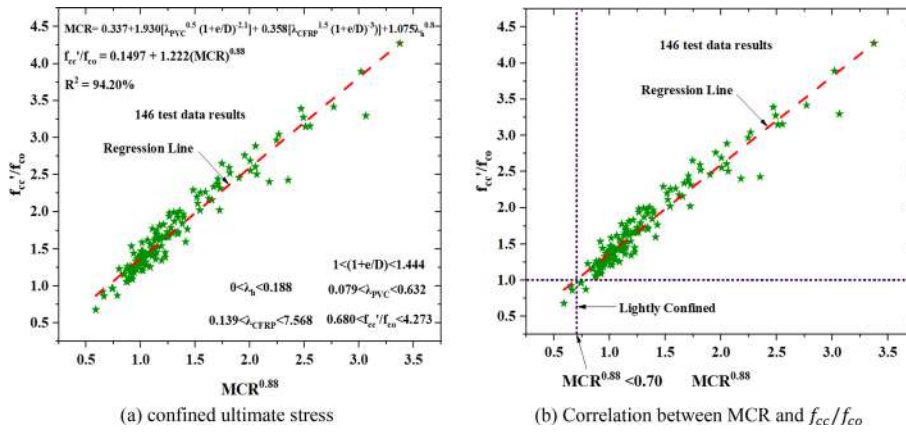


Fig. 14 Relationship between MCR and f_{cc}/f_{co} from Eqs. (7) and (8)

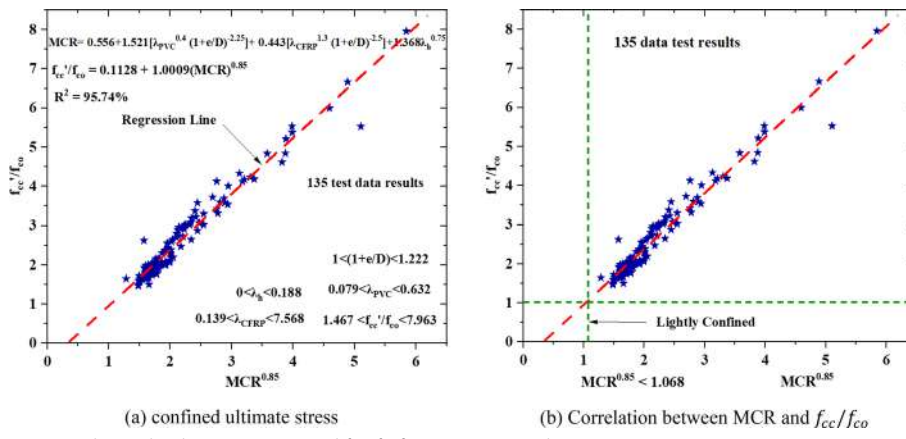


Fig. 15 Relationship between MCR and f_{cc}/f_{co} from Eqs. (12) and (13)

training, as it would constitute an ineffective use of CFRP strips for wrapping CCFPT columns.

$$\frac{f_{cc}}{f_{co}} = 0.1497 + 1.222(MCR)^{0.88} \quad (10)$$

$$MCR = 0.337 + 1.930 \left[\left(\lambda_{PVC}^{0.5} \right) \left(1 + \frac{e}{D} \right)^{-2.1} \right] + 0.358 \left[\left(\lambda_{CFRP}^{1.5} \right) \left(1 + \frac{e}{D} \right)^{-3} \right] + 1.075 \lambda_h^{0.8} \quad (11)$$

According to Isleem et al. [39], there is another group of test specimens that have a confined ratio range of 1.467–7.963, λ_{CFRP} range of 0.279–7.568, λ_{PVC} range of 0.079–0.632, λ_h range of 0–0.188, and eccentricity to diameter ratio range of 1–1.222. A multi-parameter regression analysis was conducted on a database of 135 specimens to develop Eqs. (12) and (13), as depicted in Fig. 15. The confinement ratio of CCFPT columns for other dimensionless parameters was evaluated, and the correlation coefficient R^2 was determined to be 95.74%. This relationship identifies lightly confined cases, with a

Modified Confined Ratio (MCR) less than 1.068 for 135 test data results. Hence, it is advised not to go over this limit in practice since it would signify an ineffective use of CFRP wrapping around CCFPT columns.

$$\frac{f_{cc}}{f_{co}} = 0.1128 + 1.0009(MCR)^{0.85} \quad (12)$$

$$MCR = 0.556 + 1.521 \left[\left(\lambda_{PVC}^{0.4} \right) \left(1 + \frac{e}{D} \right)^{-2.25} \right] + 0.443 \left[\left(\lambda_{CFRP}^{1.3} \right) \left(1 + \frac{e}{D} \right)^{-2.5} \right] + 1.368 \lambda_h^{0.75} \quad (13)$$

Machine learning models implemented in the present investigation

Machine learning is a subsection of artificial intelligence that relies on a large amount of input data to train algorithms and make predictions based on the input data. In this study, a total of six ML techniques has been used to predict the effects of changing the structural parameters on the performance of CCFPT columns as listed in Table 5.

Methodology

Model training and validation

In order to develop regression models, data sets are often split into training and testing sets, 80:20 or 80% of the data is utilized to train the model, and 20% is utilized for assessing it, which is the ratio of the training set to the testing set. During the training phase, the models' hyperparameters, structures, and functions are established by a trial-and-error tuning procedure. Modern ML techniques are used in the present study to predict two outputs, comprising load-carrying capacity (kN) and confined ultimate strain (mm/mm). However, the prediction for load-carrying capacity (kN) and confined ultimate strain models is not implemented directly in this study. The various ML models are combined with other models according to their individual evaluation and prognosis outputs. The combinations suggested in this study are ETR-BR, GBR-BR, XGB-LR, GBR-LR, BR-LR, and RF-LR. The models are utilized with optimized hyperparameters of individual models. Table 6 represents ideal parameters for XGB, RF, GBR, KNN models for load-carrying capacity and confined ultimate strain.

Dataset

The quantity and diversity of data used in a model's training have an enormous effect on its capacity in predicting the output parameter. In order to develop and evaluate the prediction model, the present study utilized a dataset of 216 data test results gathered through FEM simulations. Reliable regression models are developed and tested in ML utilizing input parameters that have an impact on the predicted value. In the current study, eight input parameters such as slenderness ratio (SR), confinement by PVC material (λ_{PVC}), confinement by internal hoop reinforcement (λ_h), longitudinal reinforcement to the column performance (λ_l), confinement by CFRP material (λ_{CFRP}), eccentric loading to specimen's diameter ratio (e/D), standard concrete strength (MPa) (f_o (MPa)), and area of concrete core without taking into account the longitudinal steel

Table 5 Machine learning models employed in this study

No	Model	Description
1	K-Nearest neighbor (KNN)	The KNN algorithm is based on the supervised learning approach and is one of the most basic ML algorithms. The predictions are based as a non-parametric instance-based learning system on analogies with its training data input parameters [63]. The significant hyperparameter of the model KNN is K's value. When the value of K is smaller, predictions tend to be more susceptible to individual data points, which may expose them to distortion and overfitting. A greater value of K results in smoother projections, however it may be neglected due to smaller patterns in the data [64–66]
2	Linear regression (LR)	Linear regression (LR) is well known ML classification technique used in this study and it is a straightforward supervised learning method that is particularly beneficial for forecasting an empirical response [67–70]
3	Bagging regression (BR)	The method of bagging involves two steps: aggregation and bootstrapping. It is feasible to train various models by consistently partitioning the entire dataset into smaller groups [71]. The results of the model are added together to get the final predicted values
4	XG Boost regression (XBR)	XGBoost regression refers to the use of the XGBoost algorithm for regression tasks. XGBoost, short form for extreme gradient boosting, is a popular ML algorithm known for its high predictive accuracy and efficiency. In a regression context, XGBoost is used to predict a continuous numerical output based on a set of input features or independent variables. It has gained prominence in various data science and predictive modeling applications due to its ability to handle complex relationships in the data and its robustness against overfitting [72–75]
5	Gradient boosting Regression (GBR)	Regression trees are a specific type of decision tree that are intended to estimate continuous real-valued functions rather than classifiers. The data are repeatedly separated by nodes or branches into smaller collections in order to create the regression tree. The main objective of the GBR is to incorporate numerous inadequate learners in order to increase the final estimation's precision and resilience. The GBR adjusts the contribution from the new tree utilizing an adaptation rate for avoiding problems with overfitting [76–79]
6	Random forest (RF)	A different approach ensemble technique related to boosting models is the random forest (RF) model. The random forest is one of the finest and most effective ensemble models in ML. Regression forests are used in the RF model, similarly to their use in the GBR model. The regression trees in the RF model, in contrast to the GBR model, are trained separately before their output combined to produce forecasts using self-funded data. Two key parameters must be set in need to execute the RF: the number of trees and the number of randomly selected predictor variables [80–85]

rebars (A_c (mm²)) have been considered in order to predict two output parameters (load-carrying capacity (P_{cc} (kN)) and confined concrete strain (ε_{cc} (mm/mm))).

Table 7 represents the descriptive and detailed statistical data distributions of the two output parameters. Figure 16 depicts the distributions of the output parameters such as load-carrying capacity and confined ultimate strain.

Results and discussion

Data visualization plots

Scatter plots The scatter plot is a widely used graphical tool in statistical analysis and data exploration, serving to visually illustrate the association between two variables. The conventional representation consists of a grid structure wherein each point on the graph corresponds to a distinct combination of values for the two variables being examined. In

Table 6 Optimized hyperparameters of machine learning models

	Hyperparameter	Optimized value	
		Load-carrying capacity (kN)	Confined ultimate strain (mm/mm)
XGB	N_estimators	1800	1800
	Eta	0.01	0.01
	Max_depth	5	5
	Subsample	0.5	0.5
	Colsample_bytree	1	1
KNN	N_neighbors	5	5
	Weights	Uniform	Uniform
	Leaf_size	30	30
	Algorithm	Auto	Auto
GBR	N_estimators	100	100
	Learning_rate	0.1	0.1
	Max_depth	5	5
	Max_features	Auto	Auto
RF	Max_depth	5	5
	Min_sample_split	2	2
	Max_features	Auto	Auto

Table 7 Statistical data distributions of the two output parameters

Parameter	Average	Standard deviation	Minimum	25%	50%	75%	Maximum	Kurtosis	Skewness
SR	12.236	5.608	8.000	8.000	10.000	14.000	25.000	0.684	1.437
λ_{PVC}	6.261	2.645	2.356	4.366	5.760	7.106	10.490	-0.917	0.494
λ_h	1.322	1.789	0.000	0.000	0.000	4.085	4.710	-0.847	0.963
λ_l	4.790	5.536	0.000	0.000	0.000	12.423	13.477	-1.483	0.485
λ_{CFRP}	41.315	21.725	3.973	23.839	44.699	51.084	102.16	-0.15	0.517
e/D	0.136	0.117	0.000	0.000	0.125	0.200	0.444	-0.415	0.451
f_o (MPa)	24.354	7.630	10.500	20.130	25.040	28.500	51.50	1.841	0.456
A_c (mm ²)	15952.75	7224.70	3422.57	8498.28	17019.07	19367.07	26716.92	-1.082	-0.046
ε_{cc} (mm/mm)	0.012	0.005	0.002	0.008	0.011	0.016	0.033	-0.724	0.391
P_{cc} (kN)	867.148	450.117	140.172	496.580	859.496	1163.770	2062.240	0.012	0.384

the context of graphical representation, it is customary for the horizontal axis (x-axis), to symbolize the independent variable, whereas the vertical axis (y-axis), is used to depict the dependent variable. These plots are an effective tool for displaying and analyzing datasets since each point drawn on the graph represents a single data observation. Figures 17 and 18 show the scatter plots of all the input parameters and output parameters, respectively.

Histogram Histograms play a vital role in data analysis as it visually illustrates the distribution of a single variable using a sequence of adjacent bars [86–90]. The width of each bar corresponds to a certain range of values, while the height of the bars indicates the frequency counts. In addition, these plots also provide valuable insights into meas-

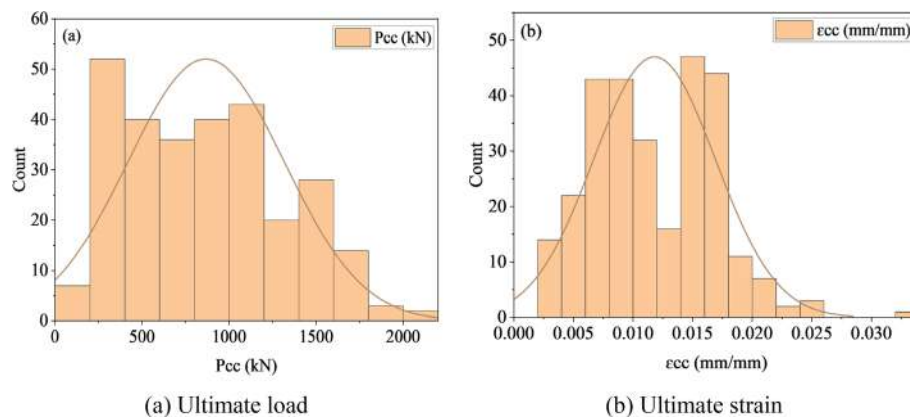


Fig. 16 Boundary histogram representing distribution of **a** load-carrying capacity and **b** confined ultimate strain

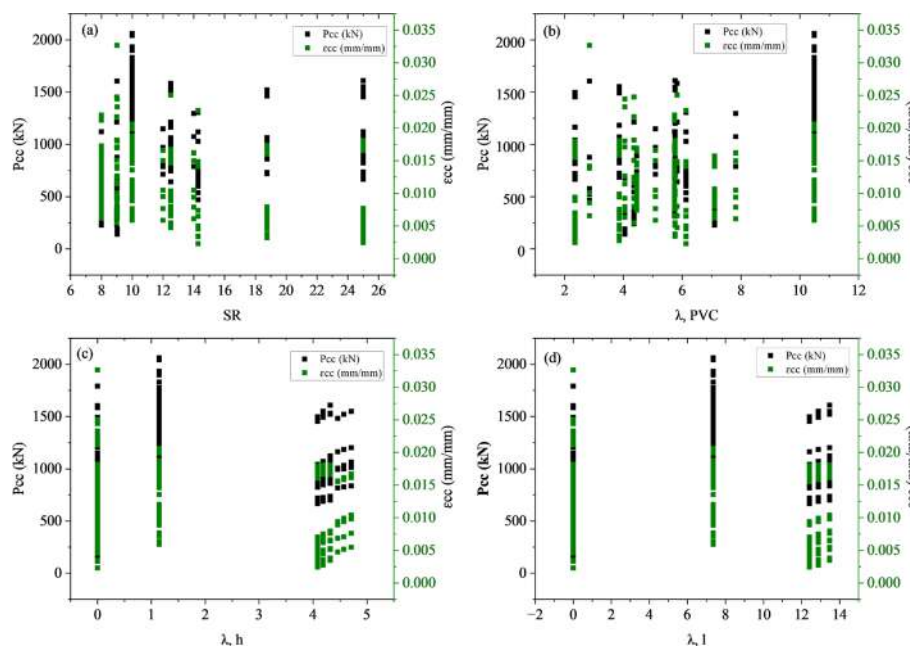


Fig. 17 Scatter plots of SR, λ_{PVC} , λ_h , λ_l for load-carrying capacity and confined ultimate strain

ures of central tendency and variability. The mode of a histogram represents the values that occur most frequently, while the width of the distribution indicates the extent of data spread. Moreover, it contributes to the identification of outliers by emphasizing data points that deviate significantly from the central distribution. Figure 19 represents the histograms of all the input parameters.

Heat map A heat map is a two-dimensional grid or map-based visual representation of data that employs colors to convey information. A gradient of colors ranging from cool to warm hues is typically used, with cooler colors representing lower values or sparse data and warmer colors representing higher values or more data concentration. The range of the color varies from -1 to 1. Understanding the color scale and interpre-

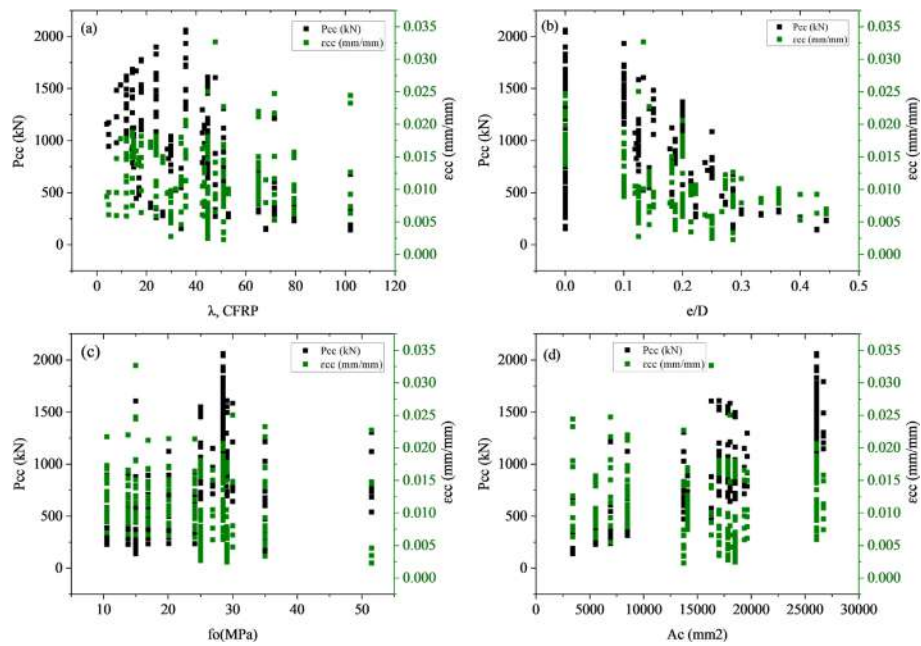


Fig. 18 Scatter plots of λ_{CFRP} , e/D , f_o , A_c for load-carrying capacity and confined ultimate strain

tation of a heat map allows for the detection of clusters, patterns, or anomalies within the data. The heatmap for load-carrying capacity and confined ultimate strain is shown in Fig. 20, respectively.

Shapley additive explanation (SHAP) analysis The significance of the input factor's impact on the predictions is elucidated by SHAP. The assessment of a model's predictions, irrespective of the specific feature, is demonstrated through the utilization of SHAP values, thereby highlighting its significance. However, it is imperative to perform this process in every possible sequence to ensure that the characteristics are evenly balanced, as the order in which a model encounters features can influence its predictions. Figure 21 depict the SHAP values for load-carrying capacity and confined ultimate strain, respectively.

Performance metrics for various algorithms

A thorough evaluation of the effectiveness indicators associated to various models utilized in the study to prognosis the two output parameters was done. These metrics are the coefficient of determination (R^2), mean square error (MSE), Root mean square error (RMSE), root relative square error (RRSE), Mean absolute error (MAE), variance account factor (VAF), Nash–Sutcliffe efficiency (NS), Kling-Gupta efficiency (KGE), and relative absolute error (RAE). Table 8 contains the equations that were utilized to evaluate these parameters.

Figures 22 and 23 illustrate the correlation between the actual values and the prognosis values of all combined models for load-carrying capacity and confined ultimate strain, respectively.

In order to prognosis the load-carrying capacity for the models used in the present investigation, NSE, KGE, and R^2 have been depicted in Fig. 24a, while RMSE, VAF,

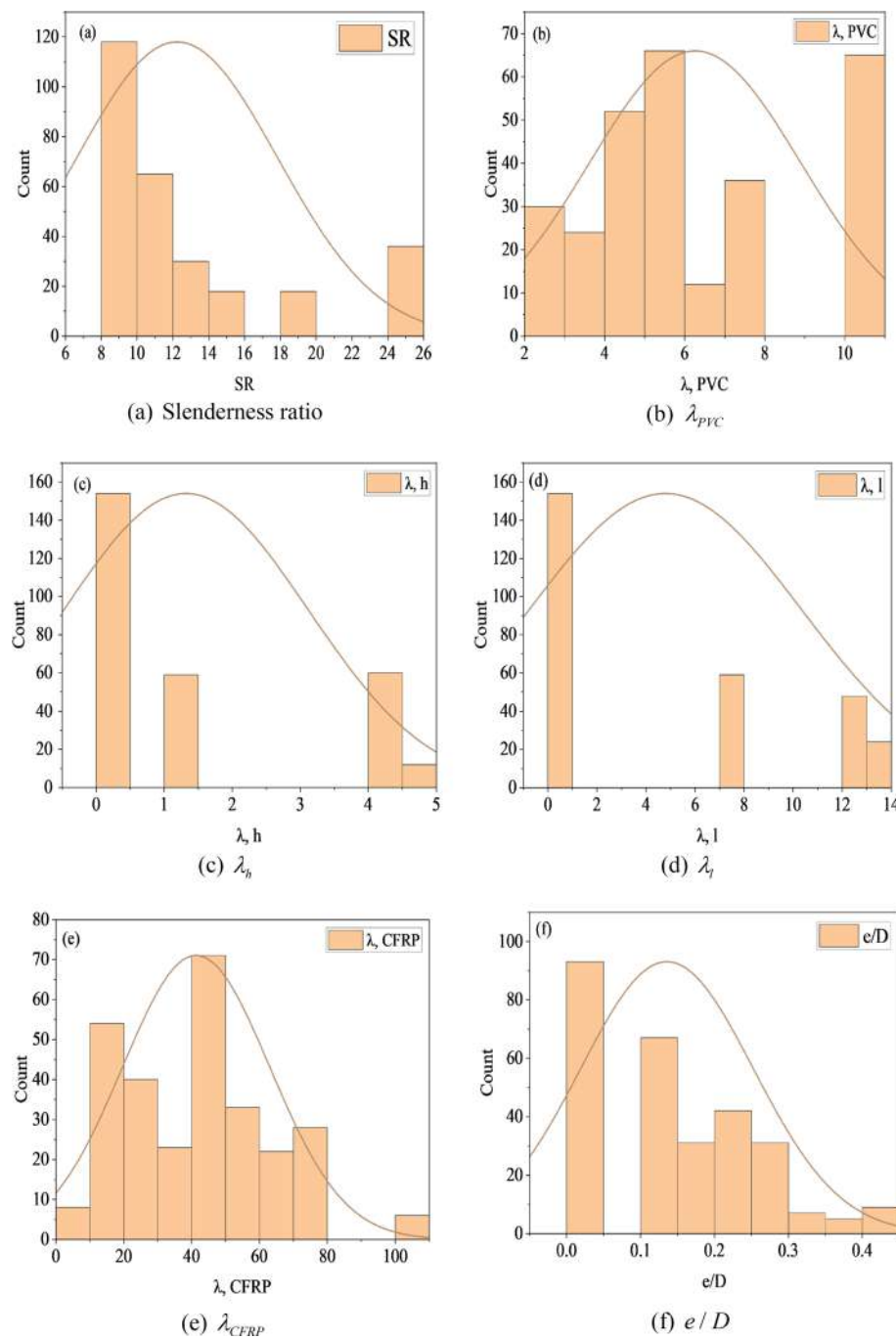


Fig. 19 Histogram representation of all input parameters

MAE, RRSE, and RAE are shown in Fig. 24b. Furthermore, MSE for load-carrying capability is shown in Fig. 24c for load-carrying capacity. In a similar manner, Fig. 25a shows the R^2 , NSE, and KGE for confined ultimate strain. RMSE, MAE and STD are represented in Fig. 25b, whereas, MSE and VAF are illustrated in Fig. 25c, d, for confined ultimate strain.

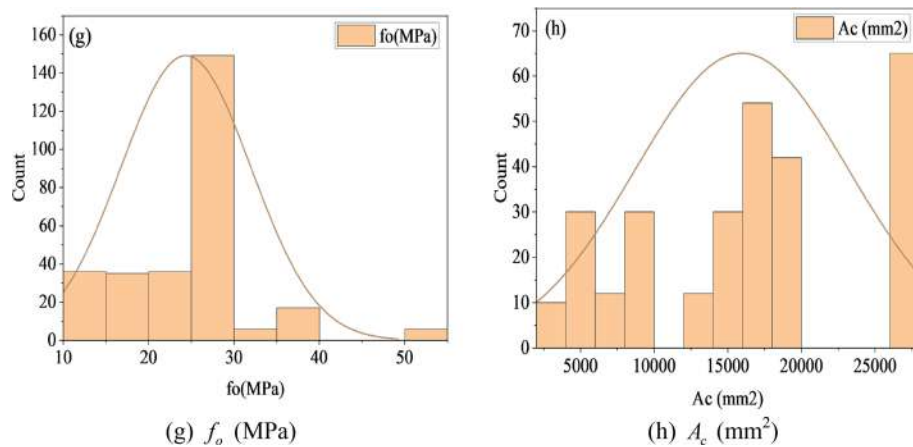
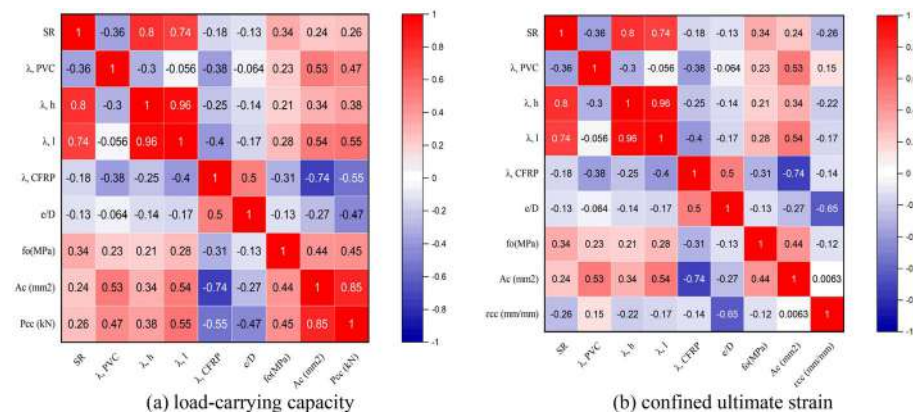
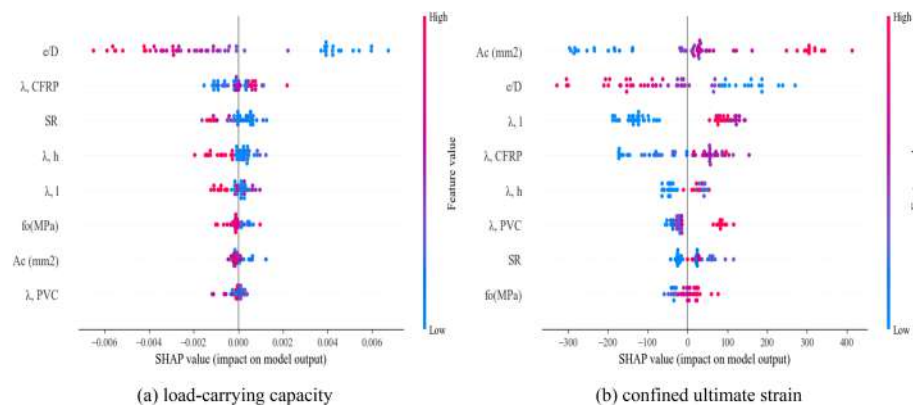
**Fig. 19** continued**Fig. 20** Heatmaps representation of input parameters with: **a** load-carrying capacity, **b** confined ultimate strain**Fig. 21** SHAP analysis values for: **a** load-carrying capacity; **b** confined ultimate strain

Table 8 Performance metrics equations

No	Parameter	Equation
1	Coefficient of determination (R^2)	$R^2 = \frac{\sum_{i=1}^P (y_i - \bar{y}_{mean})^2 - \sum_{i=1}^P (y_i - \hat{y}_i)^2}{\sum_{i=1}^P (y_i - \bar{y}_{mean})^2}$ Where y_i is the original value and \hat{y}_i is predicted value by the model, \bar{y}_{mean} is the average values and P is the number of specimens
2	Root mean square error (RMSE)	$RMSE = \sqrt{\frac{1}{P} \sum_{i=1}^P (y_i - \hat{y}_i)^2}$
3	Mean absolute error (MAE)	$MAE = \frac{1}{n} \sum_{i=1}^n y_i - \hat{y}_i $
4	Variance account factor (VAF)	$VAF = \left(1 - \frac{\text{var}(y_i - \hat{y}_i)}{\text{var}(y_i)}\right) \times 100$
5	Nash-Sutcliffe efficiency (NS)	$NS = 1 - \frac{\sum_{i=1}^n (y_i - \hat{y}_i)^2}{\sum_{i=1}^n (y_i - \bar{y}_{mean})^2}; -\infty < NS \leq 1$
6	Mean square error (MSE)	$MSE = \frac{1}{n} \sum_{i=1}^n (y_i - \hat{y}_i)^2$
7	Root relative square Error (RRSE)	$RRSE = \sqrt{\frac{\sum_{i=1}^n (y_i - \bar{y}_{mean})^2}{\sum_{i=1}^n (y_i - \hat{y}_i)^2}}$
8	Relative absolute error (RAE)	$RAE = \frac{\sum_{i=1}^n y_i - \bar{y}_{mean} ^2}{\sum_{i=1}^n (y_i - \hat{y}_i)^2}$
9	Kling-Gupta efficiency (KGE)	$KGE = 1 - \sqrt{(r - 1)^2 + (\beta - 1)^2 + (\gamma - 1)^2}$ where, r is the coefficient for correlation, β is the ratio of the average of the predicted and actual values and γ is the ratio of the standard deviation of predicted and actual values

Cross validation K-fold cross-validation is a commonly employed methodology for the purpose of optimizing hyperparameters and evaluating the effectiveness of a model where the training dataset is partitioned into 'k' subsets or folds of equal size. The model is subsequently trained 'k' times, with each iteration utilizing a distinct fold as the validation set and the remaining data as the training set. The procedure guarantees that each individual data point is utilized for validation precisely once. This approach offers a more thorough assessment compared to a single train-test split, ensuring a robust analysis. Figure 26 shows the RMSE values of all ML models for load-carrying capacity and confined ultimate strain, respectively.

Sensitivity analysis Sensitivity analysis evaluates the influence on model outputs of altering a single input separately across the whole range of possible values while preserving the nominal or base-case values of all other inputs. The sensitivity of the model to that specific input variable is defined as the variation in the model output owing to a modification in the input variable. A positive or negative percentage shift compared to the nominal answer can also be used to illustrate the sensitivity. Figure 27 represents the sensitivity analysis of all ML models for load-carrying capacity and confined ultimate strain.

Regression Error Characteristics (REC) curve The regression error characteristic (REC) curve demonstrates the percentage of predicted points that fall within the tolerance on the y-axis against the error tolerance on the x-axis. The outcome of the curve generates the error's cumulative distribution function (CDF). Regression functions can be graphically compared to one another and the null mode using REC curves. The only component that the graph changes as the reaction is scaled is the x-axis label. If a function outperforms another using the square error, it will additionally outperform

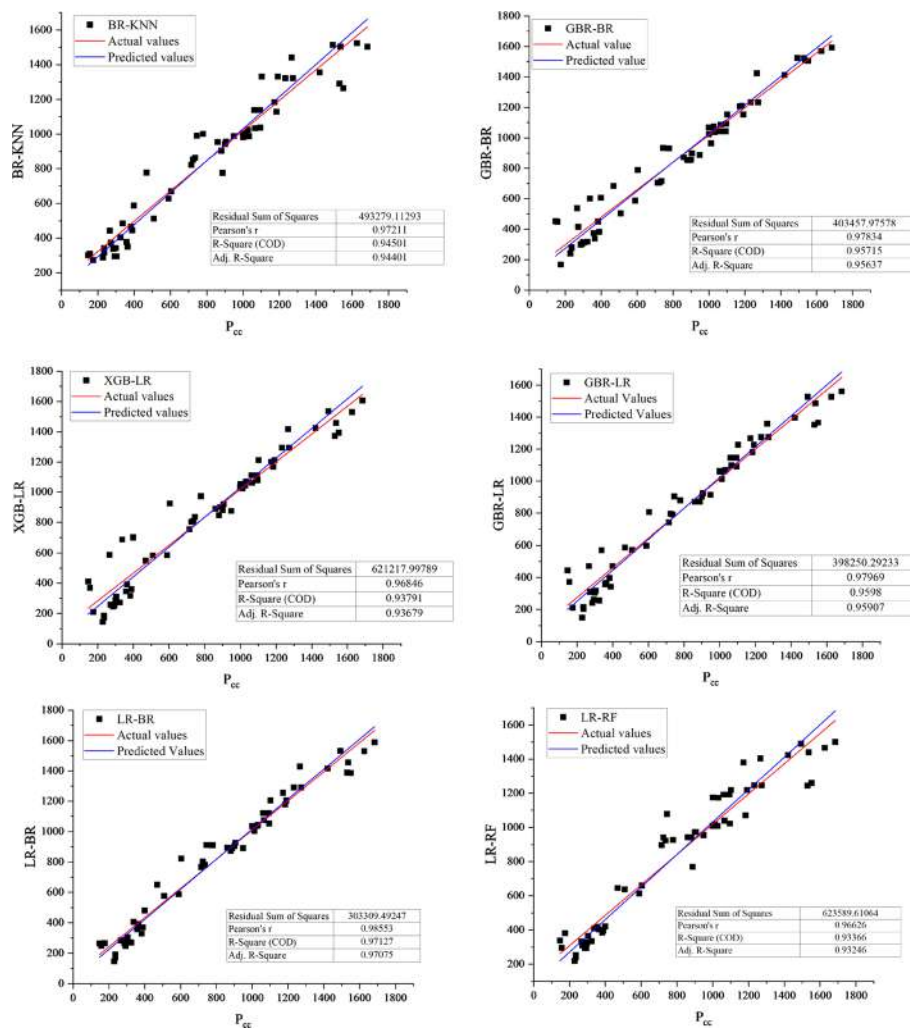


Fig. 22 Correlation between actual and prediction value of ML models for load-carrying capacity

the substitute using the absolute deviation. Figure 28 displays the REC curves of confined ultimate strain and load-carrying capacity.

Taylor diagram Taylor offered a single graphic that reviewed numerous model evaluation indices, such as the correlation coefficient and root mean square error (RMSE) values, and used to assess the effectiveness of models. By contrasting the values of the measured and predicted variables and presenting the results as a series of points on a polar plot, Taylor diagrams can demonstrate the precision of model predictions. The circumferential distance from the reference point depicts the ratio of the normalized standard deviation of the simulation from the measured values, and the azimuth angle of the plot displays the correlation coefficient between the observed and predicted values. Figure 29 depict Taylor diagrams for confined ultimate strain and load-carrying capacity, respectively. Table 9 illustrates the key comparisons between the developed model and the existing models from the literature.

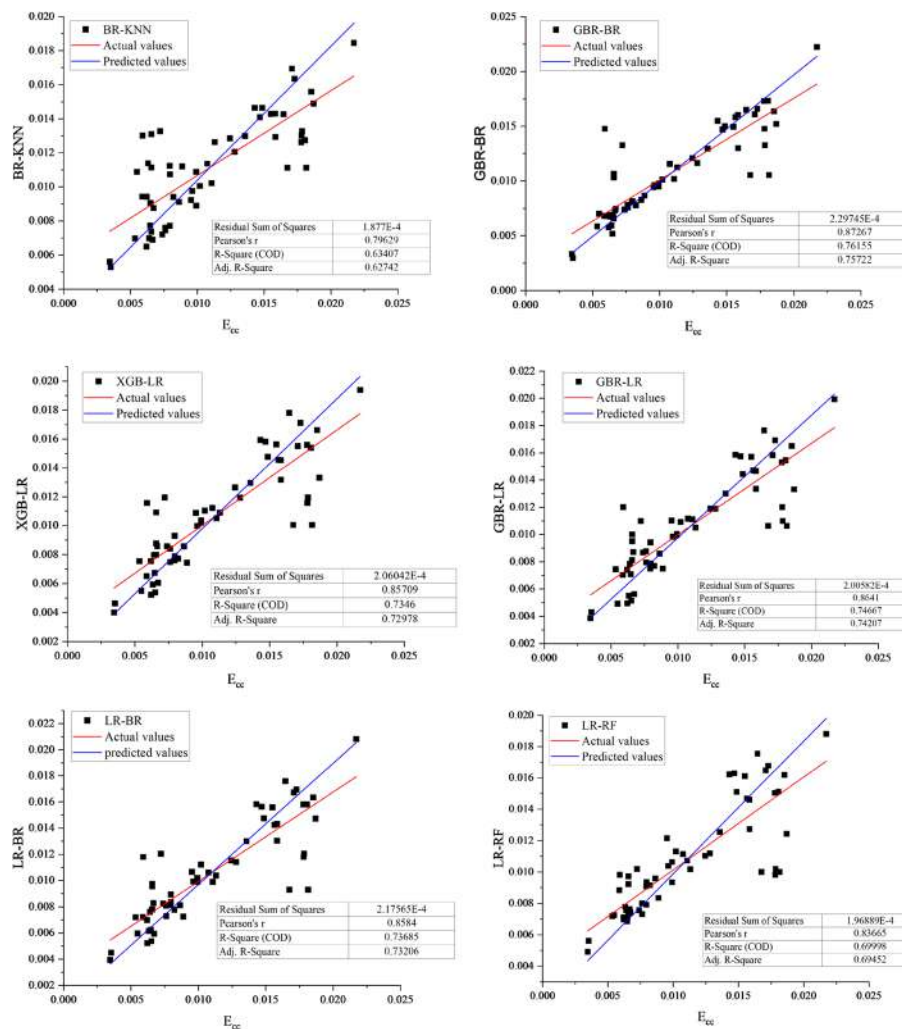


Fig. 23 Correlation between actual and prediction value of ML models for confined ultimate strain

Conclusions

This study investigates the behavior of CCFPT columns under eccentric axial compression loading. Experimental data of 32 concrete columns was collected from literature and modeled using finite element analysis. A finite element parametric study examined the effects of eccentricity, number of CFRP layers, PVC tube thickness, column slenderness ratio, CFRP spacing, confined concrete strength, and concrete core diameter on the ultimate load and strain capacities. Analytical models were developed to predict confined concrete strength and strain as functions of material properties, reinforcement parameters, and load eccentricity. Six machine learning models were employed to predict the load-carrying capacity and confined ultimate strain of the columns based on input parameters such as slenderness ratio, confinement levels, concrete strength, and cross-sectional area. The following conclusions of this study can be drawn as follows:

- 1- Increasing the load eccentricity leads to a significant reduction in the ultimate load and strain capacities of CCFPT columns.

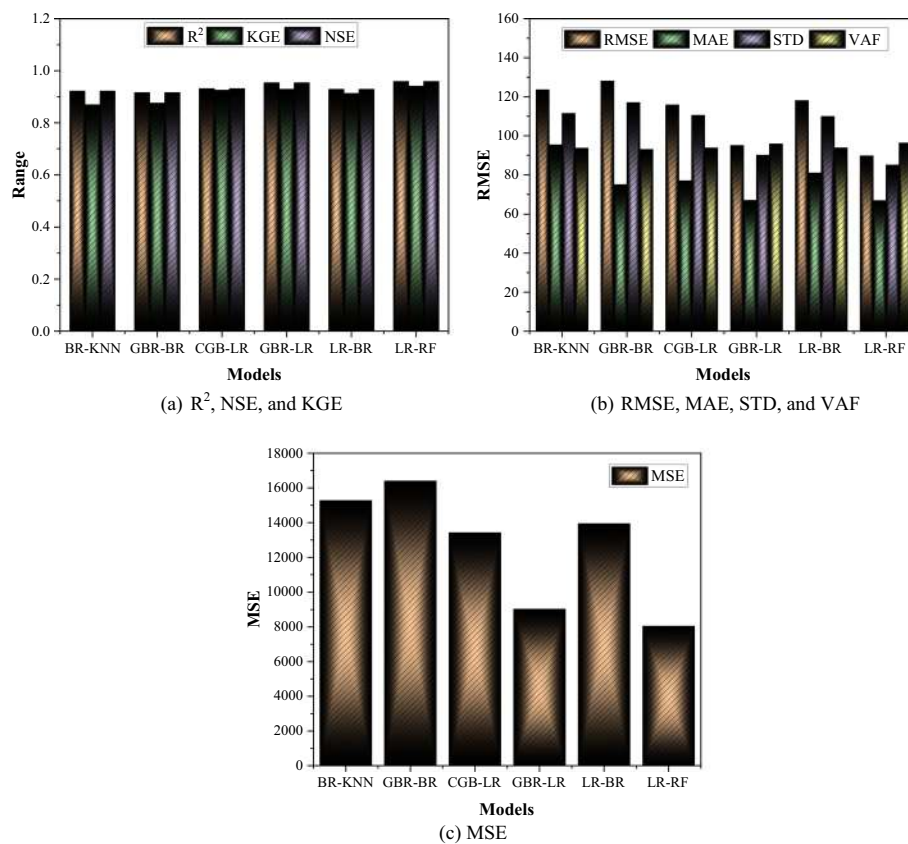


Fig. 24 Models used for the load-carrying capacity

- 2- Increasing the number of CFRP layers results in higher ultimate load and strain capacities at a given eccentricity.
- 3- Thicker PVC tubes enhance the ultimate load capacity by mitigating buckling failure, while the effect on ultimate strain is inconsistent.
- 4- Increasing the column's slenderness ratio results in lower ultimate load and strain capacities, with strain reduction being more pronounced.
- 5- Smaller spacing between CFRP strips leads to higher ultimate load and strain values.
- 6- There is an optimum range of confined concrete strength (above 15 MPa) where load and strain capacities increase more rapidly with increasing concrete strength.
- 7- Reducing the concrete core diameter decreases the ultimate load and strain capacities.
- 8- Analytical models were developed to predict the confined concrete strength and strain as functions of constituent properties such as CFRP, PVC, steel reinforcement, and load eccentricity.
- 9- The models identify thresholds of confinement parameters below which CFRP wrapping may be ineffective for confinement.
- 10- Machine learning techniques can effectively predict the load-carrying and strain capacities based on the investigated parameters.

To provide a more comprehensive understanding of the research context and to acknowledge potential constraints or challenges in the findings, it is essential to list out the limitations of the current study. Some limitations include:

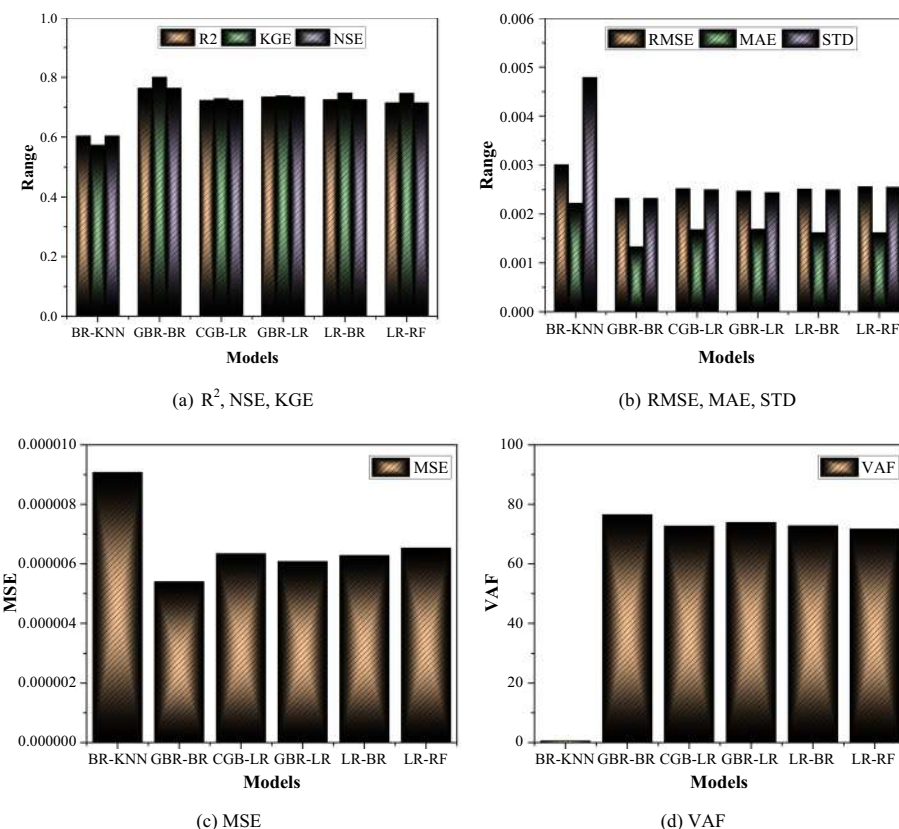


Fig. 25 Models used for the confined ultimate strain

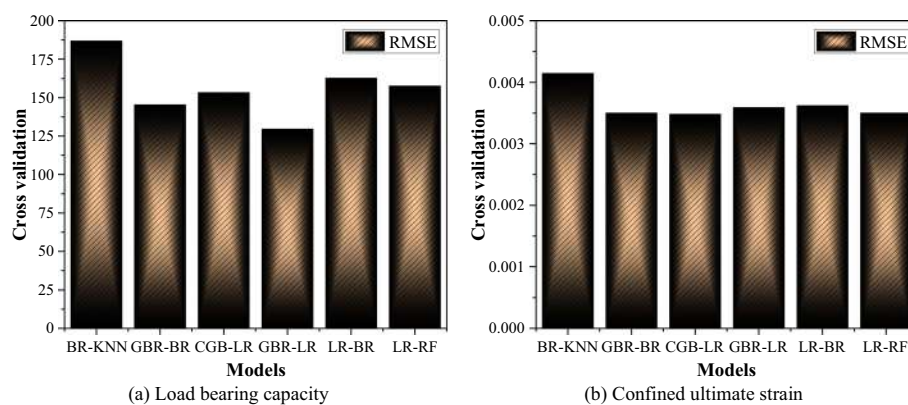


Fig. 26 RMSE values by cross validation method for: **a** Load bearing capacity; **b** confined ultimate strain

- 1- The accuracy of the results is limited by the assumptions and simplifications made in the finite element modeling approach.
- 2- The study only considers CCFPT columns under eccentric axial compression loading. The behavior under other loading conditions such as flexure, cyclic loading, etc. is not addressed.

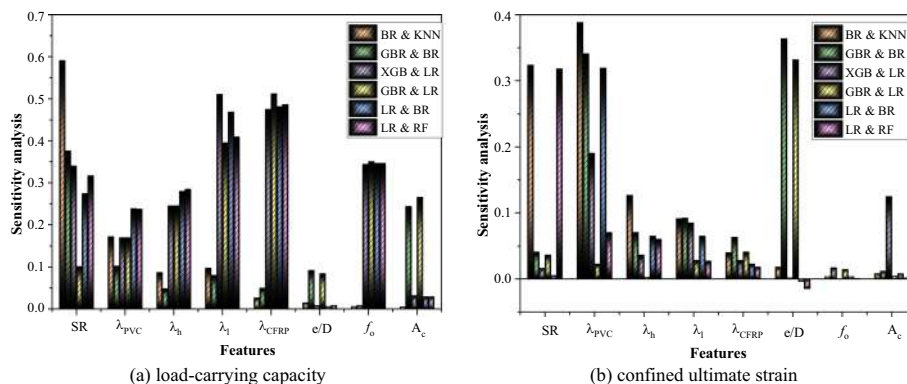


Fig. 27 Sensitivity analysis of ML models for: **a** load-carrying capacity; **b** confined ultimate strain

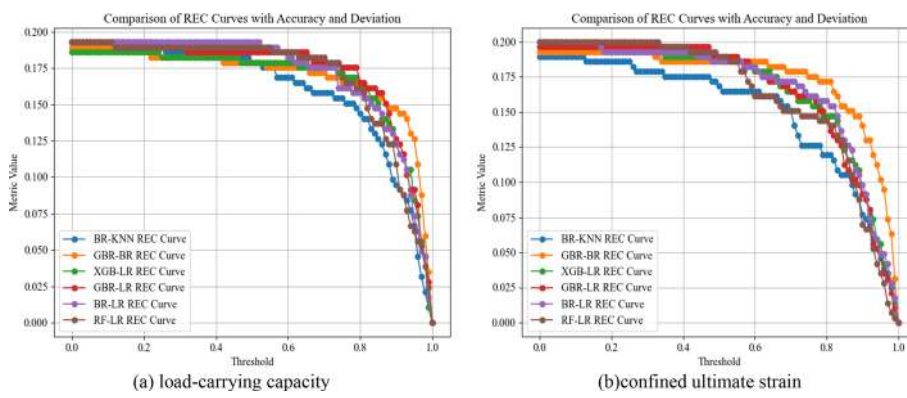


Fig. 28 REC curve analysis of all ML models for: **a** load-carrying capacity; **b** confined ultimate strain

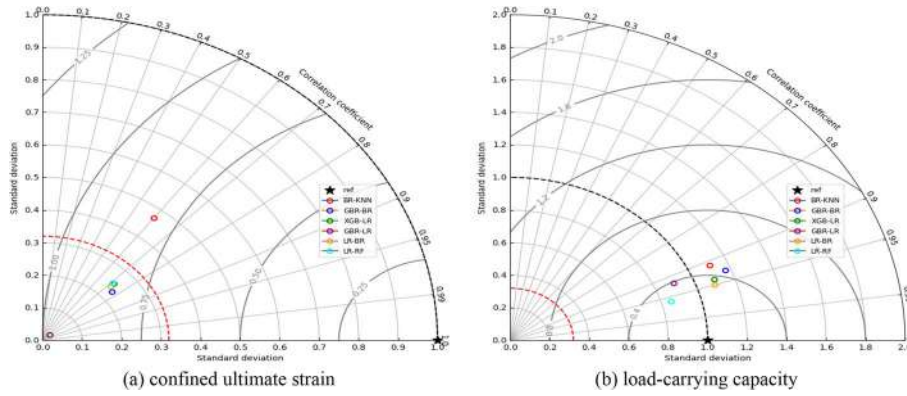


Fig. 29 Taylor diagrams of all ML models for: **a** confined ultimate strain; **b** load-carrying capacity

- 3- The study focuses only on specific input parameters such as slenderness ratio, confinement levels, etc. There may be other factors influencing the behavior of CCFPT columns that are not considered.
- 4- The study is focused on circular CCFPT columns only. The conclusions may not be directly extensible to non-circular cross-sections.
- 5- The study is computational in nature and does not involve any physical experiments or validations, which could be considered a limitation.

Table 9 Comparison between the developed model of this study and the existing models

Aspect	This study	Existing models	Remarks
Confined concrete compressive strength to unconfined concrete compressive strength ratio (f_{cc}/f_{co})	Equations (10) and (12) expressing f_{cc}/f_{co} as functions of dimensionless PVC, CFRP, steel, and eccentricity parameters	Previous models did not explicitly account for these dimensionless parameters and their interaction effects	Identifies thresholds of confinement parameters ($MCR < 0.7$ or 1.068) below which CFRP wrapping may be ineffective, not captured in previous models
Confined concrete strain to unconfined concrete strain ratio ($\epsilon_{cc}/\epsilon_{co}$)	Equations (11) and (13) expressing $\epsilon_{cc}/\epsilon_{co}$ as functions of dimensionless PVC, CFRP, steel, and eccentricity parameters	Previous models did not explicitly consider these combined effects	–
Effect of load eccentricity	Reduction in confinement efficiency with higher load eccentricity	Consistent with previous studies [55]	–
Load-strain response	Decreasing capacity with increasing CFRP hoop spacing	Agrees with prior studies [9, 60]	–
Effect of CFRP layers	Increase in capacities with higher number of CFRP layers	Matches previous findings [56]	–
Effect of PVC thickness	Increase in capacities with higher PVC thickness	Aligns with studies showing reduced buckling failure [57]	–
Machine learning modeling	Employing six ML techniques	Previous models did not explicitly apply ML algorithms	–

The current study focused solely on CFRP-PVC confined concrete columns under eccentric axial compression loading, without considering all possible loading scenarios in practice. Crucial loading scenarios such as long-term sustained loading, combined axial-flexural loading, shear, torsion, cyclic/seismic loading, dynamic and impact loading, pure flexure, and environmental factors were not examined. Future research should include cyclic lateral loading tests to simulate seismic actions, shear and torsional capacity studies, especially for short columns or beam-column joints, combined axial-flexural loading tests to develop interaction diagrams, and flexural behavior analysis using four-point bending tests and finite element modeling. Additionally, long-term creep and fatigue tests, impact resistance and dynamic response under high strain-rate loading conditions, and the impact of environmental exposure on performance under different loading conditions should be investigated. This future research will help us understand the effects of various loading scenarios, such as strain-rate dependent material behavior under dynamic and impact loading, creep deformations under long-term loading, degradation of concrete core and debonding of CFRP strips under cyclic loading, various failure modes under shear and torsional loads, and material property degradation due to environmental factors.

Appendix

See Table 10.

Table 10 Summary of simulated database of concrete-filled PVC tube columns confined with CFRP under uniaxial eccentric compression

Group	No	Authors	f'_c (MPa)	CFRP	Geometrical properties			FEM results						
					No. of layers	Thickness of one layer (mm)	Total thickness, (mm)	D (mm)	H (mm)	t_p (mm)	D_c (mm)	e (mm)	CFRP spacing (mm)	
												Reinforcement	Longitudinal (mm 2)	
												Hoop (mm 2)	P_{fp} (kN)	
												ϵ_{fp} (mm/mm)		
G1	1	Feng and Diao (2013)	298	3	0.1650	0.4950	200	500	7.8	1844	20	20	28.3	1711.00 0.0112941
2	2	Fang et al. (2020)	28.5	3	0.1650	0.4950	200	500	7.8	1844	20	20	0.0	1491.61 0.01138
3	3	Chang et al. (2021)	29.0	3	0.1650	0.4950	168	588	5.0	158.0	20	20	0.0	1074.14 0.0104865
4	4	Guo et al. (2008)	26.9	3	0.1650	0.4950	165	495	4.0	157.0	20	20	0.0	970.39 0.010498
5	5	Bandyopadhyay et al. (2020)	29.3	3	0.1650	0.4950	160	500	2.3	155.4	20	20	28.3	1163.77 0.0093917
6	6	Bandyopadhyay et al. (2020)	29.3	3	0.1650	0.4950	160	500	3.7	152.6	20	20	28.3	1183.98 0.0099209
7	7	Bandyopadhyay et al. (2020)	29.3	3	0.1650	0.4950	160	500	5.4	149.2	20	20	28.3	1201.70 0.0103924
8	8	Bandyopadhyay et al. (2020)	28.8	3	0.1650	0.4950	160	1000	2.3	155.4	20	20	28.3	999.66 0.0066642
9	9	Bandyopadhyay et al. (2020)	28.8	3	0.1650	0.4950	160	1000	3.7	152.6	20	20	28.3	1027.13 0.0073854
10	10	Bandyopadhyay et al. (2020)	28.8	3	0.1650	0.4950	160	1000	5.4	149.2	20	20	28.3	1039.39 0.0076868
11	11	Bandyopadhyay et al. (2020)	33.1	3	0.1650	0.4950	160	1000	2.3	155.4	20	20	28.3	1038.99 0.0060802

Table 10 (continued)

Group	No	Authors	f'_c (MPa)	CFRP	Geometrical properties				ϵ (mm)	CFRP spacing (mm)	Reinforcement Longitudinal (mm)	FEM results		
					No. of layers	Thickness of one layer (mm)	Total thickness (mm)	D (mm)	H (mm)	t_p (mm)	D_c (mm)	P_{FP} (kN)	ϵ_{FP} (mm/mm)	
12	Bandyopadhyay et al. (2020)	33.1	3	0.1650	0.4950	160	1000	3.7	152.6	20	78.6	28.3	1070.76	0.0069247
13	Bandyopadhyay et al. (2020)	33.1	3	0.1650	0.4950	160	1000	5.4	149.2	20	78.6	28.3	1095.43	0.0076154
14	Bandyopadhyay et al. (2020)	28.8	3	0.1650	0.4950	160	750	2.3	155.4	20	78.6	28.3	1042.34	0.0070276
15	Bandyopadhyay et al. (2020)	28.8	3	0.1650	0.4950	160	750	3.7	152.6	20	78.6	28.3	1052.58	0.0075237
16	Bandyopadhyay et al. (2020)	28.8	3	0.1650	0.4950	160	750	5.4	149.2	20	78.6	28.3	1065.17	0.0079495
17	Wolde-mariam et al. (2019)	10.5	3	0.1650	0.4950	90	180	3.0	84.0	20	20	0.0	359.12	0.0106936
18	Wolde-mariam et al. (2019)	10.5	3	0.1650	0.4950	110	220	3.0	104.0	20	20	0.0	482.86	0.0150426
19	Wolde-mariam et al. (2019)	10.5	3	0.1650	0.4950	140	280	3.0	134.0	20	20	0.0	700.57	0.0127416
20	Wolde-mariam et al. (2019)	13.8	3	0.1650	0.4950	90	180	3.0	84.0	20	20	0.0	362.00	0.0104215
21	Wolde-mariam et al. (2019)	13.8	3	0.1650	0.4950	110	220	3.0	104.0	20	20	0.0	484.26	0.0141641

Table 10 (continued)

Group	No.	Authors	f'_c (MPa)	CFRP	Geometrical properties				ϵ (mm)	CFRP spacing (mm)	Reinforcement Longitudinal (mm 2)	P_{FP} (kN)	ϵ_{FP} (mm/mm)	FEM results	
					No. of layers	Thickness of one layer (mm)	Total thickness, (mm)	D (mm)	H (mm)	t_p (mm)	D_c (mm)				
22	Woldemariam et al.(2019)	13.8	3	0.1650	0.4950	140	280	3.0	134.0	20	20	0.0	0.0	700.36	0.0123339
23	Woldemariam et al.(2019)	16.9	3	0.1650	0.4950	90	180	3.0	84.0	20	20	0.0	0.0	364.37	0.0102039
24	Woldemariam et al.(2019)	16.9	3	0.1650	0.4950	110	220	3.0	104.0	20	20	0.0	0.0	492.38	0.0137836
25	Woldemariam et al.(2019)	16.9	3	0.1650	0.4950	140	280	3.0	134.0	20	20	0.0	0.0	709.03	0.0124357
26	Woldemariam et al.(2019)	20.1	3	0.1650	0.4950	90	180	3.0	84.0	20	20	0.0	0.0	369.81	0.010031
27	Wolde-mariam et al. (2019)	20.1	3	0.1650	0.4950	110	220	3.0	104.0	20	20	0.0	0.0	496.58	0.0134881
28	Wolde-mariam et al. (2019)	20.1	3	0.1650	0.4950	140	280	3.0	134.0	20	20	0.0	0.0	699.81	0.0119766
29	Wolde-mariam et al. (2019)	24.1	3	0.1650	0.4950	90	180	3.0	84.0	20	20	0.0	0.0	374.92	0.0099464
30	Wolde-mariam et al. (2019)	24.1	3	0.1650	0.4950	110	220	3.0	104.0	20	20	0.0	0.0	504.49	0.0132098
31	Wolde-mariam et al. (2019)	24.1	3	0.1650	0.4950	140	280	3.0	134.0	20	20	0.0	0.0	739.04	0.0120551
32	Alatshyan et al. (2022)	15.0	3	0.1650	0.4950	70	158	2.0	66.0	20	20	0.0	0.0	190.30	0.0126406
33	Alatshyan et al. (2022)	15.0	3	0.1650	0.4950	100	225	3.0	94.0	20	20	0.0	0.0	370.99	0.0150797

Table 10 (continued)

Group	No.	Authors	f'_c (MPa)	CFRP	Geometrical properties				ϵ (mm)	CFRP spacing (mm)	Reinforcement (mm \times mm 2)	FEM results			
					No. of layers	Thickness of one layer (mm)	Total thickness, (mm)	D (mm)	H (mm)	t_p (mm)	D_c (mm)	P_{FP} (kN)	ϵ_{FP} (mm/mm)		
34	Alatshyan et al. (2022)	15.0	3	0.1650	0.4950	150	338	3.0	144.0	20	20	0.0	1605.78	0.032649	
35	Alatshyan et al. (2022)	35.0	3	0.1650	0.4950	70	158	2.0	66.0	20	20	0.0	676.56	0.0735143	
36	Alatshyan et al. (2022)	35.0	3	0.1650	0.4950	100	225	3.0	94.0	20	20	0.0	1213.93	0.080108	
37	Gupta et al. (2013)	35.0	3	0.1650	0.4950	140	500	3.9	132.2	20	20	0.0	739.83	0.0073812	
38	Gupta et al. (2013)	300	3	0.1650	0.4950	160	500	4.3	151.5	20	20	0.0	1585.03	0.0250326	
39	Gupta et al. (2013)	51.5	3	0.1650	0.4950	140	500	3.9	132.2	20	20	0.0	1306.36	0.0227229	
G2	40 Feng and Ditaq (2013)	29.8	3	0.1650	0.4950	200	500	7.8	184.4	30	20	78.6	28.3	1483.36	0.0088606
41	Fang et al. (2020)	28.5	3	0.1650	0.4950	200	500	7.8	184.4	30	20	0.0	0.0	1305.05	0.0090631
42	Chang et al. (2021)	29.0	3	0.1650	0.4950	168	588	5.0	158.0	30	20	0.0	0.0	919.91	0.0078878
43	Guo et al. (2008)	26.9	3	0.1650	0.4950	165	495	4.0	157.0	30	20	0.0	833.83	0.0076548	
44	Bandyopadhyay et al. (2020)	29.3	3	0.1650	0.4950	160	500	2.3	155.4	30	20	78.6	28.3	992.93	0.0068703
45	Bandyopadhyay et al. (2020)	29.3	3	0.1650	0.4950	160	500	3.7	152.6	30	20	78.6	28.3	997.15	0.007076
46	Bandyopadhyay et al. (2020)	29.3	3	0.1650	0.4950	160	500	5.4	149.2	30	20	78.6	28.3	1012.06	0.0076207

Table 10 (continued)

Group	No.	Authors	f'_c (MPa)	CFRP	Geometrical properties			ϵ (mm)	CFRP spacing (mm)	Reinforcement	FEM results				
					No. of layers	Thickness of one layer (mm)	Total thickness (mm)				Longitudinal (mm)	Hoop (mm) ²	P_{FP} (kN)	ϵ_{FP} (mm/mm)	
47	Bandyopadhyay et al. (2020)	28.8	3	0.1650	0.4950	160	1000	2.3	155.4	30	20	786	28.3	822.75	0.0041756
48	Bandyopadhyay et al. (2020)	28.8	3	0.1650	0.4950	160	1000	3.7	152.6	30	20	786	28.3	847.00	0.0048291
49	Bandyopadhyay et al. (2020)	28.8	3	0.1650	0.4950	160	1000	5.4	149.2	30	20	786	28.3	859.50	0.0051647
50	Bandyopadhyay et al. (2020)	33.1	3	0.1650	0.4950	160	1000	2.3	155.4	30	20	786	28.3	860.41	0.0037957
51	Bandyopadhyay et al. (2020)	33.1	3	0.1650	0.4950	160	1000	3.7	152.6	30	20	786	28.3	880.47	0.0044471
52	Bandyopadhyay et al. (2020)	33.1	3	0.1650	0.4950	160	1000	5.4	149.2	30	20	786	28.3	901.75	0.005116
53	Bandyopadhyay et al. (2020)	28.8	3	0.1650	0.4950	160	750	2.3	155.4	30	20	786	28.3	861.02	0.00459
54	Bandyopadhyay et al. (2020)	28.8	3	0.1650	0.4950	160	750	3.7	152.6	30	20	786	28.3	868.63	0.0050188
55	Bandyopadhyay et al. (2020)	28.8	3	0.1650	0.4950	160	750	5.4	149.2	30	20	786	28.3	870.78	0.0052652
56	Woldenariam et al. (2019)	10.5	3	0.1650	0.4950	90	180	3.0	84.0	30	20	0.0	0.0	285.53	0.0086324

Table 10 (continued)

Group	No.	Authors	f'_c (MPa)	CFRP	Geometrical properties			FEM results				
					No. of layers	Thickness of one layer (mm)	Total thickness, (mm)	D (mm)	H (mm)	t_p (mm)	D_c (mm)	ϵ (mm)
57	Wolde-nariam et al. (2019)	10.5	3	0.1650	0.4950	110	220	3.0	104.0	30	20	0.0
58	Wolde-nariam et al. (2019)	10.5	3	0.1650	0.4950	140	280	3.0	134.0	30	20	0.0
59	Wolde-nariam et al. (2019)	13.8	3	0.1650	0.4950	90	180	3.0	84.0	30	20	0.0
60	Wolde-nariam et al. (2019)	13.8	3	0.1650	0.4950	110	220	3.0	104.0	30	20	0.0
61	Wolde-nariam et al. (2019)	13.8	3	0.1650	0.4950	140	280	3.0	134.0	30	20	0.0
62	Wolde-nariam et al. (2019)	16.9	3	0.1650	0.4950	90	180	3.0	84.0	30	20	0.0
63	Wolde-nariam et al. (2019)	16.9	3	0.1650	0.4950	110	220	3.0	104.0	30	20	0.0
64	Wolde-nariam et al. (2019)	16.9	3	0.1650	0.4950	140	280	3.0	134.0	30	20	0.0
65	Wolde-nariam et al. (2019)	20.1	3	0.1650	0.4950	90	180	3.0	84.0	30	20	0.0
66	Wolde-nariam et al. (2019)	20.1	3	0.1650	0.4950	110	220	3.0	104.0	30	20	0.0

Table 10 (continued)

Group	No	Authors	f'_c (MPa)	CFRP	Geometrical properties				e(mm)	CFRP spacing (mm)	Reinforcement Longitudinal (mm)	FEM results			
					No. of layers	Thickness of one layer (mm)	Total thickness, (mm)	D (mm)	H (mm)	t_p (mm)	D_c (mm)				
67	Wolde-nariam et al. (2019)	20.1	3	0.1650	0.4950	140	280	3.0	134.0	30	20	0.0	594.00	0.0097809	
68	Wolde-nariam et al. (2019)	24.1	3	0.1650	0.4950	90	180	3.0	84.0	30	20	0.0	301.62	0.0080043	
69	Wolde-nariam et al. (2019)	24.1	3	0.1650	0.4950	110	220	3.0	104.0	30	20	0.0	409.81	0.010128	
70	Wolde-nariam et al. (2019)	24.1	3	0.1650	0.4950	140	280	3.0	134.0	30	20	0.0	613.27	0.0091505	
71	Alatshani et al. (2022)	150	3	0.1650	0.4950	70	158	2.0	66.0	30	20	0.0	140.17	0.0092653	
72	Alatshani et al. (2022)	150	3	0.1650	0.4950	100	225	3.0	94.0	30	20	0.0	295.15	0.0116233	
73	Alatshani et al. (2022)	150	3	0.1650	0.4950	150	338	3.0	144.0	30	20	0.0	576.64	0.0085399	
74	Alatshani et al. (2022)	35.0	3	0.1650	0.4950	70	158	2.0	66.0	30	20	0.0	146.85	0.0063302	
75	Alatshani et al. (2022)	35.0	3	0.1650	0.4950	100	225	3.0	94.0	30	20	0.0	337.16	0.0079382	
76	Gupta et al. (2013)	35.0	3	0.1650	0.4950	140	500	3.9	132.2	30	20	0.0	599.90	0.0050255	
77	Gupta et al. (2013)	30.0	3	0.1650	0.4950	160	500	4.3	151.5	30	20	0.0	779.00	0.0065801	
78	Gupta et al. (2013)	51.5	3	0.1650	0.4950	140	500	3.9	132.2	30	20	0.0	683.85	0.0034637	
G3	Feng and Ditao (2013)	29.8	3	0.1650	0.4950	200	500	7.8	184.4	40	20	78.6	28.3	1305.57	0.00730019

Table 10 (continued)

Group	No	Authors	f'_c (MPa)	CFRP	Geometrical properties				e (mm)	CFRP spacing (mm)	Reinforcement	FEM results		
					No. of layers	Thickness of one layer (mm)	Total thickness, (mm)	D (mm)	H (mm)	t_p (mm)	D_c (mm)	P_{FP} (kN)	ϵ_{FP} (mm/mm)	
80	Fang et al. (2020)	28.5	3	0.1650	0.4950	200	500	7.8	184.4	40	20	0.0	0.0	1146.19 0.00741328
81	Chang et al. (2021)	29.0	3	0.1650	0.4950	168	588	5.0	158.0	40	20	0.0	0.0	787.696 0.0060925
82	Guo et al. (2008)	26.9	3	0.1650	0.4950	165	495	4.0	157.0	40	20	0.0	0.0	714.675 0.0058764
83	Bandyopadhyay et al. (2020)	29.3	3	0.1650	0.4950	160	500	2.3	155.4	40	20	786	28.3	816.817 0.00473508
84	Bandyopadhyay et al. (2020)	29.3	3	0.1650	0.4950	160	500	3.7	152.6	40	20	786	28.3	825 0.00516044
85	Bandyopadhyay et al. (2020)	29.3	3	0.1650	0.4950	160	500	5.4	149.2	40	20	786	28.3	836.378 0.00548913
86	Bandyopadhyay et al. (2020)	28.8	3	0.1650	0.4950	160	1000	2.3	155.4	40	20	786	28.3	666.373 0.00267053
87	Bandyopadhyay et al. (2020)	28.7	3	0.1650	0.4950	160	1000	3.7	152.6	40	20	786	28.3	686.559 0.00314402
88	Bandyopadhyay et al. (2020)	28.7	3	0.1650	0.4950	160	1000	5.4	149.2	40	20	786	28.3	699.247 0.00347773
89	Bandyopadhyay et al. (2020)	33.1	3	0.1650	0.4950	160	1000	2.3	155.4	40	20	786	28.3	695.082 0.00244965
90	Bandyopadhyay et al. (2020)	33.0	3	0.1650	0.4950	160	1000	3.7	152.6	40	20	786	28.3	714.253 0.00287348

Table 10 (continued)

Group	No	Authors	f'_c (MPa)	CFRP	Geometrical properties			e (mm)	CFRP spacing (mm)	Reinforcement (mm)	FEM results	
					No. of layers	Thickness of one layer (mm)	Total thickness, (mm)				P_{FP} (kN)	ϵ_{FP} (mm/mm)
91	Bandyopadhyay et al. (2020)	330	3	0.1650	0.4950	160	1000	5.4	149.2	40	20	786
92	Bandyopadhyay et al. (2020)	28.8	3	0.1650	0.4950	160	750	2.3	155.4	40	20	786
93	Bandyopadhyay et al. (2020)	28.7	3	0.1650	0.4950	160	750	3.7	152.6	40	20	786
94	Bandyopadhyay et al. (2020)	28.6	3	0.1650	0.4950	160	750	5.4	149.2	40	20	786
95	Wolde-mariam et al. (2019)	10.5	3	0.1650	0.4950	90	180	3.0	84.0	40	20	0.0
96	Wolde-mariam et al. (2019)	10.5	3	0.1650	0.4950	110	220	3.0	104.0	40	20	0.0
97	Wolde-mariam et al. (2019)	10.5	3	0.1650	0.4950	140	280	3.0	134.0	40	20	0.0
98	Wolde-mariam et al. (2019)	13.8	3	0.1650	0.4950	90	180	3.0	84.0	40	20	0.0
99	Wolde-mariam et al. (2019)	13.8	3	0.1650	0.4950	110	220	3.0	104.0	40	20	0.0
100	Wolde-mariam et al. (2019)	13.8	3	0.1650	0.4950	140	280	3.0	134.0	40	20	0.0

Table 10 (continued)

Group	No	Authors	f'_c (MPa)	CFRP	Geometrical properties			e (mm)	CFRP spacing (mm)	Reinforcement (mm)	FEM results		
					No. of layers	Thickness of one layer (mm)	Total thickness, (mm)				P_{FP} (kN)	ϵ_{FP} (mm/mm)	
101	Woldemariam et al. (2019)	16.9	3	0.1650	0.4950	90	180	3.0	84.0	40	20	0.0	232.019 0.00662505
102	Woldemariam et al.(2019)	16.9	3	0.1650	0.4950	110	220	3.0	104.0	40	20	0.0	324.062 0.00887621
103	Woldemariam et.al(2019)	16.9	3	0.1650	0.4950	140	280	3.0	134.0	40	20	0.0	500.525 0.00835778
104	Woldemariam et.al(2019)	20.1	3	0.1650	0.4950	90	180	3.0	84.0	40	20	0.0	235.975 0.00651312
105	Woldemariam et.al(2019)	20.1	3	0.1650	0.4950	110	220	3.0	104.0	40	20	0.0	327.878 0.0084092
106	Woldemariam et.al(2019)	20.1	3	0.1650	0.4950	140	280	3.0	134.0	40	20	0.0	503.701 0.00803535
107	Woldemariam et.al(2019)	24.1	3	0.1650	0.4950	90	180	3.0	84.0	40	20	0.0	235.418 0.00621365
108	Woldemariam et.al(2019)	24.1	3	0.1650	0.4950	110	220	3.0	104.0	40	20	0.0	332.746 0.00784926
109	Woldemariam et.al(2019)	24.1	3	0.1650	0.4950	140	280	3.0	134.0	40	20	0.0	520.438 0.007445
110	Alatshani et.al. (2022)	15.0	3	0.1650	0.4950	100	225	3.0	94.0	40	20	0.0	237.966 0.00922308
111	Alatshani et.al. (2022)	15.0	3	0.1650	0.4950	150	338	3.0	144.0	40	20	0.0	468.647 0.00658042
112	Alatshani et.al. (2022)	35.0	3	0.1650	0.4950	100	225	3.0	94.0	40	20	0.0	266.395 0.00548428
113	Gupta et.al. (2013)	35.0	3	0.1650	0.4950	140	500	3.9	132.2	40	20	0.0	470.638 0.00333277

Table 10 (continued)

Group	No	Authors	f'_c (MPa)	CFRP	Geometrical properties			e (mm)	CFRP spacing (mm)	Reinforcement (mm)	FEM results		
					No. of layers	Thickness of one layer (mm)	Total thickness, (mm)	D (mm)	H (mm)	t_p (mm)	D_c (mm)	P_{FP} (kN)	ϵ_{FP} (mm/mm)
	114	Gupta et al. (2013)	30.0	3	0.1650	0.4950	160	500	4.3	151.5	40	20	0.0
	115	Gupta et al. (2013)	51.5	3	0.1650	0.4950	140	500	3.9	1322	40	20	0.0
G4	116	Feng and Diao (2013)	29.8	3	0.1650	0.4950	200	500	7.8	1844	0	20	786
	117	Fang et al. (2020)	28.5	3	0.1650	0.4950	200	500	7.8	1844	0	20	0.0
	118	Chang et al. (2021)	29.0	3	0.1650	0.4950	168	588	5.0	1580	0	20	0.0
	119	Guo et al. (2008)	26.9	3	0.1650	0.4950	165	495	4.0	157.0	0	20	0.0
	120	Bandyopadhyay et al. (2020)	29.3	3	0.1650	0.4950	160	500	2.3	155.4	0	20	786
	121	Bandyopadhyay et al. (2020)	29.3	3	0.1650	0.4950	160	500	3.7	152.6	0	20	786
	122	Bandyopadhyay et al. (2020)	29.2	3	0.1650	0.4950	160	500	5.4	149.2	0	20	786
	123	Bandyopadhyay et al. (2020)	28.8	3	0.1650	0.4950	160	1000	2.3	155.4	0	20	786
	124	Bandyopadhyay et al. (2020)	28.7	3	0.1650	0.4950	160	1000	3.7	152.6	0	20	786

Table 10 (continued)

Group	No.	Authors	f'_c (MPa)	CFRP	Geometrical properties			e (mm)	CFRP spacing (mm)	Reinforcement	FEM results				
					No. of layers	Thickness of one layer (mm)	Total thickness, (mm)				P_{FP} (kN)	Hoop (mm 2)	ϵ_{FP} (mm/mm)		
125	Bandyopadhyay et al. (2020)	286	3	0.1650	0.4950	160	1000	5.4	149.2	0	20	786	28.3	1529.69	0.0180706
126	Bandyopadhyay et al. (2020)	33.1	3	0.1650	0.4950	160	1000	2.3	155.4	0	20	786	28.3	1496.38	0.0177091
127	Bandyopadhyay et al. (2020)	33.0	3	0.1650	0.4950	160	1000	3.7	152.6	0	20	786	28.3	1551.55	0.0177804
128	Bandyopadhyay et al. (2020)	33.0	3	0.1650	0.4950	160	1000	5.4	149.2	0	20	786	28.3	1609.04	0.0176577
129	Bandyopadhyay et al. (2020)	288	3	0.1650	0.4950	160	750	2.3	155.4	0	20	786	28.3	1463.6	0.0160323
130	Bandyopadhyay et al. (2020)	287	3	0.1650	0.4950	160	750	3.7	152.6	0	20	786	28.3	1492.81	0.0166546
131	Bandyopadhyay et al. (2020)	286	3	0.1650	0.4950	160	750	5.4	149.2	0	20	786	28.3	1521.62	0.0170457
132	Wolde-mariam et al. (2019)	10.5	3	0.1650	0.4950	90	180	3.0	84.0	0	20	0.0	0.0	532.097	0.0157054
133	Wolde-mariam et al. (2019)	10.5	3	0.1650	0.4950	110	220	3.0	104.0	0	20	0.0	0.0	665.995	0.0217241
134	Wolde-mariam et al. (2019)	10.5	3	0.1650	0.4950	140	280	3.0	134.0	0	20	0.0	0.0	895.004	0.016771

Table 10 (continued)

Group	No.	Authors	f'_c (MPa)	CFRP	Geometrical properties			ϵ (mm)	CFRP spacing (mm)	Reinforcement	FEM results			
					No. of layers	Thickness of one layer (mm)	Total thickness (mm)				P_{FP} (kN)	ϵ_{FP} (mm/mm)		
135	Wolde-mariam et al. (2019)	13.8	3	0.1650	0.4950	90	180	3.0	84.0	0	20	0.0	526.103	0.0152845
136	Wolde-mariam et al. (2019)	13.8	3	0.1650	0.4950	110	220	3.0	104.0	0	20	0.0	683.044	0.0219888
137	Wolde-mariam et al. (2019)	13.8	3	0.1650	0.4950	140	280	3.0	134.0	0	20	0.0	888.009	0.0164584
138	Wolde-mariam et al. (2019)	16.9	3	0.1650	0.4950	90	180	3.0	84.0	0	20	0.0	520.834	0.014848
139	Wolde-mariam et al. (2019)	16.9	3	0.1650	0.4950	110	220	3.0	104.0	0	20	0.0	680.341	0.0211653
140	Wolde-mariam et al. (2019)	16.9	3	0.1650	0.4950	140	280	3.0	134.0	0	20	0.0	892.155	0.0166974
141	Wolde-mariam et al. (2019)	20.1	3	0.1650	0.4950	90	180	3.0	84.0	0	20	0.0	536.017	0.0151161
142	Wolde-mariam et al. (2019)	20.1	3	0.1650	0.4950	110	220	3.0	104.0	0	20	0.0	686.368	0.0214186
143	Wolde-mariam et al. (2019)	20.1	3	0.1650	0.4950	140	280	3.0	134.0	0	20	0.0	892.567	0.0169387
144	Wolde-mariam et al. (2019)	24.1	3	0.1650	0.4950	90	180	3.0	84.0	0	20	0.0	543.057	0.0153472

Table 10 (continued)

Group	No	Authors	f'_c (MPa)	CFRP	Geometrical properties			CFRP spacing (mm)	Reinforcement Longitudinal (mm)	FEM results				
					No. of layers	Thickness of one layer (mm)	Total thickness, (mm)							
145	Wolde-mariam et al. (2019)	24.1	3	0.1650	0.4950	110	220	3.0	1040	0	0.0	692.822	0.0213791	
146	Wolde-mariam et al. (2019)	24.1	3	0.1650	0.4950	140	280	3.0	134.0	0	0.0	0.0	918.09	0.0164578
147	Alatshen et al. (2022)	15.0	3	0.1650	0.4950	70	158	2.0	66.0	0	0.0	0.0	319.343	0.0244225
148	Alatshen et al. (2022)	15.0	3	0.1650	0.4950	100	225	3.0	94.0	0	0.0	0.0	544.34	0.0247487
149	Alatshen et al. (2022)	15.0	3	0.1650	0.4950	150	338	3.0	144.0	0	0.0	0.0	878.351	0.0141953
150	Alatshen et al. (2022)	35.0	3	0.1650	0.4950	70	158	2.0	66.0	0	0.0	0.0	323.741	0.0232614
151	Alatshen et al. (2022)	35.0	3	0.1650	0.4950	100	225	3.0	94.0	0	0.0	0.0	603.988	0.0217165
152	Gupta et al. (2013)	35.0	3	0.1650	0.4950	140	500	3.9	132.2	0	0.0	0.0	1027.51	0.0141492
153	Gupta et al. (2013)	30.0	3	0.1650	0.4950	160	500	4.3	151.5	0	0.0	0.0	1212.46	0.0146498
154	Gupta et al. (2013)	51.5	3	0.1650	0.4950	140	500	3.9	132.2	0	0.0	0.0	1120.82	0.0145217
G5	Feng and Dittao (2013)	298	1	0.1650	0.1650	200	500	7.8	184.4	0	0.0	28.3	1493.19	0.0154932
156	Fang et al. (2020)	285	1	0.1650	0.1650	200	500	7.8	184.4	0	0.0	0.0	1206.31	0.0149269
157	Chang et al. (2021)	29.0	1	0.1650	0.1650	168	588	5.0	158.0	0	0.0	0.0	918.539	0.0149933

Table 10 (continued)

Group	No.	Authors	f'_c (MPa)	CFRP	Geometrical properties			ϵ (mm)	CFRP spacing (mm)	Reinforcement (mm 2)	FEM results	
					No. of layers	Thickness of one layer (mm)	Total thickness, (mm)				P_{FP} (kN)	ϵ_{FP} (mm/mm 2)
158	Guo et al. (2008)	269	1	0.1650	0.1650	165	495	4.0	157.0	0	20	0.0
159	Bandyopadhyay et al. (2020)	293	1	0.1650	0.1650	160	500	2.3	155.4	0	20	78.6
160	Bandyopadhyay et al. (2020)	293	1	0.1650	0.1650	160	500	3.7	152.6	0	20	78.6
161	Bandyopadhyay et al. (2020)	292	1	0.1650	0.1650	160	500	5.4	149.2	0	20	78.6
162	Bandyopadhyay et al. (2020)	288	1	0.1650	0.1650	160	1000	2.3	155.4	0	20	78.6
163	Bandyopadhyay et al. (2020)	287	1	0.1650	0.1650	160	1000	3.7	152.6	0	20	78.6
164	Bandyopadhyay et al. (2020)	286	1	0.1650	0.1650	160	1000	5.4	149.2	0	20	78.6
165	Bandyopadhyay et al. (2020)	33.1	1	0.1650	0.1650	160	1000	2.3	155.4	0	20	78.6
166	Bandyopadhyay et al. (2020)	33.0	1	0.1650	0.1650	160	1000	3.7	152.6	0	20	78.6
167	Bandyopadhyay et al. (2020)	33.0	1	0.1650	0.1650	160	1000	5.4	149.2	0	20	78.6

Table 10 (continued)

Group	No	Authors	f'_c (MPa)	CFRP	Geometrical properties			ϵ (mm)	CFRP spacing (mm)	FEM results					
					No. of layers	Thickness of one layer (mm)	Total thickness, (mm)			Longitudinal	Hoop (mm 2)				
168	Bandyopadhyay et al. (2020)	288	1	0.1650	0.1650	160	750	2.3	155.4	0	20	786	28.3	974.089	0.0165982
169	Bandyopadhyay et al. (2020)	287	1	0.1650	0.1650	160	750	3.7	152.6	0	20	786	28.3	1004.17	0.0173276
170	Bandyopadhyay et al. (2020)	286	1	0.1650	0.1650	160	750	5.4	149.2	0	20	786	28.3	1039.31	0.0171347
171	Woldemariam et al. (2019)	105	1	0.1650	0.1650	90	180	3.0	84.0	0	20	0.0	0.0	275.945	0.0146221
172	Woldemariam et al. (2019)	105	1	0.1650	0.1650	110	220	3.0	104.0	0	20	0.0	0.0	357.827	0.0172831
173	Woldemariam et al. (2019)	105	1	0.1650	0.1650	140	280	3.0	134.0	0	20	0.0	0.0	479.019	0.0145736
174	Woldemariam et al. (2019)	13.8	1	0.1650	0.1650	90	180	3.0	84.0	0	20	0.0	0.0	279.842	0.0141469
175	Woldemariam et al. (2019)	13.8	1	0.1650	0.1650	110	220	3.0	104.0	0	20	0.0	0.0	367.305	0.0165749
176	Woldemariam et al. (2019)	13.8	1	0.1650	0.1650	140	280	3.0	134.0	0	20	0.0	0.0	490.926	0.0142936
177	Woldemariam et al. (2019)	16.9	1	0.1650	0.1650	90	180	3.0	84.0	0	20	0.0	0.0	290.591	0.0144222
178	Woldemariam et al. (2019)	16.9	1	0.1650	0.1650	110	220	3.0	104.0	0	20	0.0	0.0	382.247	0.0168312

Table 10 (continued)

Group	No	Authors	f'_c (MPa)	CFRP	Geometrical properties			ϵ (mm)	CFRP spacing (mm)	Reinforcement (mm)	FEM results		
					No. of layers	Thickness of one layer (mm)	Total thickness, (mm)				P_{Fp} (kN)	ϵ_{Fp} (mm/mm ²)	
179	Woldemariam et al. (2019)	16.9	1	0.1650	0.1650	140	280	3.0	134.0	0	20	0.0	502.993 0.0146488
180	Woldemariam et al. (2019)	20.1	1	0.1650	0.1650	90	180	3.0	84.0	0	20	0.0	304.005 0.0146907
181	Woldemariam et al. (2019)	20.1	1	0.1650	0.1650	110	220	3.0	104.0	0	20	0.0	391.818 0.0171532
182	Woldemariam et al. (2019)	20.1	1	0.1650	0.1650	140	280	3.0	134.0	0	20	0.0	508.595 0.0143099
183	Woldemariam et al. (2019)	24.1	1	0.1650	0.1650	90	180	3.0	84.0	0	20	0.0	313.672 0.015021
184	Woldemariam et al. (2019)	24.1	1	0.1650	0.1650	110	220	3.0	104.0	0	20	0.0	398.467 0.0164454
185	Woldemariam et al. (2019)	24.1	1	0.1650	0.1650	140	280	3.0	134.0	0	20	0.0	547.351 0.0145212
186	Alatshani et al. (2022)	15.0	1	0.1650	0.1650	70	158	2.0	66.0	0	20	0.0	153.103 0.018004
187	Alatshani et al. (2022)	15.0	1	0.1650	0.1650	100	225	3.0	94.0	0	20	0.0	259.762 0.0181604
188	Alatshani et al. (2022)	15.0	1	0.1650	0.1650	150	338	3.0	144.0	0	20	0.0	444.219 0.0138528
189	Alatshani et al. (2022)	35.0	1	0.1650	0.1650	70	158	2.0	66.0	0	20	0.0	175.388 0.0170836
190	Alatshani et al. (2022)	35.0	1	0.1650	0.1650	100	225	3.0	94.0	0	20	0.0	347.331 0.0169558

Table 10 (continued)

Group	No.	Authors	f'_c (MPa)	CFRP	Geometrical properties			e (mm)	CFRP Spacing (mm)	Reinforcement			FEM results			
					No. of layers	Thickness of one layer (mm)	Total thickness (mm)			D (mm)	H (mm)	t_p (mm)	D_c (mm)	Longitudinal (mm)	Hoop (mm)	P_{FP} (kN)
	191	Gupta et al. (2013)	35.0	1	0.1650	0.1650	140	500	3.9	132.2	0	20	0.0	0.0	641.981	0.0148607
	192	Gupta et al. (2013)	30.0	1	0.1650	0.1650	160	500	4.3	151.5	0	20	0.0	0.0	744.98	0.0148598
	193	Gupta et al. (2013)	51.5	1	0.1650	0.1650	140	500	3.9	132.2	0	20	0.0	0.0	767.403	0.0147855
G6	194	Feng and Diao (2013)	29.8	2	0.1650	0.3300	200	500	7.8	184.4	20	20	786	28.3	1483.3	0.0105532
	195	Fang et al. (2020)	28.5	2	0.1650	0.3300	200	500	7.8	184.4	20	20	0.0	0.0	1266.78	0.0107531
	196	Chang et al. (2021)	29.0	2	0.1650	0.3300	168	588	5.0	158.0	20	20	0.0	0.0	917.251	0.00941262
	197	Guo et al. (2008)	26.9	2	0.1650	0.3300	165	495	4.0	157.0	20	20	0.0	0.0	8284.15	0.00952826
	198	Bandyopadhyay et al. (2020)	29.3	2	0.1650	0.3300	160	500	2.3	155.4	20	20	786	28.3	1005.26	0.00888699
	199	Bandyopadhyay et al. (2020)	29.3	2	0.1650	0.3300	160	500	3.7	152.6	20	20	786	28.3	1022.91	0.00942246
	200	Bandyopadhyay et al. (2020)	29.2	2	0.1650	0.3300	160	500	5.4	149.2	20	20	786	28.3	1041.2	0.00982598
	201	Bandyopadhyay et al. (2020)	28.8	2	0.1650	0.3300	160	1000	2.3	155.4	20	20	786	28.3	860.553	0.00534356
	202	Bandyopadhyay et al. (2020)	28.7	2	0.1650	0.3300	160	1000	3.7	152.6	20	20	786	28.3	880.082	0.00619547

Table 10 (continued)

Group	No	Authors	f'_c (MPa)	CFRP	Geometrical properties			FEM results				
					No. of layers	Thickness of one layer (mm)	Total thickness, (mm)	D (mm)	H (mm)	t_p (mm)	D_c (mm)	ϵ (mm)
203	Bandyopadhyay et al. (2020)	286	2	0.1650	0.3300	160	1000	5.4	149.2	20	20	28.3
204	Bandyopadhyay et al. (2020)	33.1	2	0.1650	0.3300	160	1000	2.3	155.4	20	20	28.3
205	Bandyopadhyay et al. (2020)	33.0	2	0.1650	0.3300	160	1000	3.7	152.6	20	20	28.3
206	Bandyopadhyay et al. (2020)	33.0	2	0.1650	0.3300	160	1000	5.4	149.2	20	20	28.3
207	Bandyopadhyay et al. (2020)	28.8	2	0.1650	0.3300	160	750	2.3	155.4	20	20	28.3
208	Bandyopadhyay et al. (2020)	28.7	2	0.1650	0.3300	160	750	3.7	152.6	20	20	28.3
209	Bandyopadhyay et al. (2020)	28.6	2	0.1650	0.3300	160	750	5.4	149.2	20	20	28.3
210	Wolde-mariam et al. (2019)	105	2	0.1650	0.3300	90	180	3.0	84.0	20	20	0.0
211	Wolde-mariam et al. (2019)	105	2	0.1650	0.3300	110	220	3.0	104.0	20	20	0.0
212	Wolde-mariam et al. (2019)	105	2	0.1650	0.3300	140	280	3.0	134.0	20	20	0.0

Table 10 (continued)

Group	No	Authors	f'_c (MPa)	CFRP	Geometrical properties				e (mm)	CFRP spacing (mm)	Reinforcement	FEM results		
					No. of layers	Thickness of one layer (mm)	Total thickness, (mm)	D (mm)	H (mm)	t_p (mm)	D_c (mm)	P_{FP} (kN)	ϵ_{FP} (mm/mm)	
213	Wolde-mariam et al. (2019)	13.8	2	0.1650	0.3300	90	180	3.0	84.0	20	20	0.0	282.212	0.0100281
214	Wolde-mariam et al. (2019)	13.8	2	0.1650	0.3300	110	220	3.0	104.0	20	20	0.0	382.494	0.0128031
215	Wolde-mariam et al. (2019)	13.8	2	0.1650	0.3300	140	280	3.0	134.0	20	20	0.0	551.835	0.0115052
216	Wolde-mariam et al. (2019)	16.9	2	0.1650	0.3300	90	180	3.0	84.0	20	20	0.0	285.031	0.00973412
217	Wolde-mariam et al. (2019)	16.9	2	0.1650	0.3300	110	220	3.0	104.0	20	20	0.0	393.756	0.0125451
218	Wolde-mariam et al. (2019)	16.9	2	0.1650	0.3300	140	280	3.0	134.0	20	20	0.0	563.121	0.0116135
219	Wolde-mariam et al. (2019)	20.1	2	0.1650	0.3300	90	180	3.0	84.0	20	20	0.0	293.533	0.00962472
220	Wolde-mariam et al. (2019)	20.1	2	0.1650	0.3300	110	220	3.0	104.0	20	20	0.0	1122.04	0.0814981
221	Wolde-mariam et al. (2019)	20.1	2	0.1650	0.3300	140	280	3.0	134.0	20	20	0.0	561.646	0.011143
222	Wolde-mariam et al. (2019)	24.1	2	0.1650	0.3300	90	180	3.0	84.0	20	20	0.0	297.383	0.00934479

Table 10 (continued)

Group	No.	Authors	f'_c (MPa)	CFRP	Geometrical properties			FEM results				
					No. of layers	Thickness of one layer (mm)	Total thickness, (mm)	D (mm)	H (mm)	t_p (mm)	D_c (mm)	ϵ (mm)
223	Voldemariam et.al.(2019)	24.1	2	0.1650	0.3300	110	220	3.0	104.0	20	20	0.0
224	Voldemariam et.al.(2019)	24.1	2	0.1650	0.3300	140	280	3.0	134.0	20	20	0.0
225	Alatshani et.al. (2022)	15.0	2	0.1650	0.3300	70	158	2.0	66.0	20	20	0.0
226	Alatshani et.al. (2022)	15.0	2	0.1650	0.3300	100	225	3.0	94.0	20	20	0.0
227	Alatshani et.al. (2022)	15.0	2	0.1650	0.3300	150	338	3.0	144.0	20	20	0.0
228	Alatshani et.al. 350 (2022)	35.0	2	0.1650	0.3300	70	158	2.0	66.0	20	20	0.0
229	Alatshani et.al. (2022)	35.0	2	0.1650	0.3300	100	225	3.0	94.0	20	20	0.0
230	Gupta et.al. (2013)	35.0	2	0.1650	0.3300	140	500	3.9	132.2	20	20	0.0
231	Gupta et.al. (2013)	30.0	2	0.1650	0.3300	160	500	4.3	151.5	20	20	0.0
232	Gupta et.al. (2013)	51.5	2	0.1650	0.3300	140	500	3.9	132.2	20	20	0.0
G7	Feng and Ditao (2013)	29.8	3	0.1650	0.4950	200	500	7.8	184.4	20	30	78.6
234	Feng and Ditao (2013)	29.8	3	0.1650	0.4950	200	500	7.8	184.4	20	40	78.6
235	Feng and Ditao (2013)	29.8	3	0.1650	0.4950	200	500	7.8	184.4	20	50	78.6
236	Feng and Ditao (2013)	29.8	3	0.1650	0.4950	200	500	7.8	184.4	20	60	78.6

Table 10 (continued)

Group	No	Authors	f'_c (MPa)	CFRP	Geometrical properties			CFRP spacing (mm)	Reinforcement (mm)	FEM results				
					No. of layers	Thickness of one layer (mm)	Total thickness, (mm)			P_{fp} (kN)	ϵ_{fp} (mm/mm)			
237	Feng and Diao (2013)	29.8	3	0.1650	0.4950	200	500	7.8	184.4	40	30	28.3	1232.38	0.00722051
238	Feng and Diao (2013)	29.8	3	0.1650	0.4950	200	500	7.8	184.4	40	40	28.3	1146.17	0.00642979
239	Feng and Diao (2013)	29.8	3	0.1650	0.4950	200	500	7.8	184.4	40	50	28.3	1118.03	0.00749183
240	Feng and Diao (2013)	29.8	3	0.1650	0.4950	200	500	7.8	184.4	40	60	28.3	1060.83	0.00590467
241	Feng and Diao (2013)	29.8	1	0.1650	0.1650	200	500	7.8	184.4	20	30	28.3	1227.13	0.00948638
242	Feng and Diao (2013)	29.8	1	0.1650	0.1650	200	500	7.8	184.4	20	50	28.3	1172.28	0.00953031
243	Feng and Diao (2013)	29.8	1	0.1650	0.1650	200	500	7.8	184.4	20	60	28.3	1158.17	0.00887273
244	Feng and Diao (2013)	29.8	1	0.1650	0.1650	200	500	7.8	184.4	40	30	28.3	979.47	0.00595941
245	Feng and Diao (2013)	29.8	1	0.1650	0.1650	200	500	7.8	184.4	40	50	28.3	944.408	0.00609346
246	Feng and Diao (2013)	29.8	3	0.1650	0.4950	200	500	7.8	184.4	30	30	28.3	1398.26	0.00891455
247	Feng and Diao (2013)	29.8	3	0.1650	0.4950	200	500	7.8	184.4	30	50	28.3	1267.69	0.00955223
248	Feng and Diao (2013)	29.8	3	0.1650	0.4950	200	500	7.8	184.4	30	60	28.3	1195.32	0.00728488
249	Feng and Diao (2013)	29.8	3	0.1650	0.4950	200	500	7.8	184.4	50	30	28.3	1085.9	0.00590829
250	Feng and Diao (2013)	29.8	1	0.1650	0.1650	200	500	7.8	184.4	30	50	28.3	1059.16	0.00766278

Table 10 (continued)

Group	No.	Authors	f'_c (MPa)	CFRP	Geometrical properties				e (mm)	CFRP spacing (mm)	Reinforcement	FEM results			
					No. of layers	Thickness of one layer (mm)	Total thickness, (mm)	D (mm)	H (mm)	t_p (mm)	D_c (mm)	Longitudinal (mm 2)	Hoop (mm 2)	P_{FP} (kN)	ϵ_{FP} (mm/mm)
251	Feng and Diao (2013)	29.8	3	0.1650	0.4950	200	500	7.8	184.4	0	30	78.6	28.3	1898.15	0.0162354
252	Feng and Diao (2013)	29.8	3	0.1650	0.4950	200	500	7.8	184.4	0	40	78.6	28.3	1764.72	0.0148901
253	Feng and Diao (2013)	29.8	3	0.1650	0.4950	200	500	7.8	184.4	0	50	78.6	28.3	1683.92	0.0185209
254	Feng and Diao (2013)	29.8	3	0.1650	0.4950	200	500	7.8	184.4	0	60	78.6	28.3	1617.42	0.014679
255	Feng and Diao (2013)	29.8	2	0.1650	0.3300	200	500	7.8	184.4	0	30	78.6	28.3	1667.94	0.0159197
256	Feng and Diao (2013)	29.8	2	0.1650	0.3300	200	500	7.8	184.4	0	40	78.6	28.3	1579.04	0.0149141
257	Feng and Diao (2013)	29.8	2	0.1650	0.3300	200	500	7.8	184.4	0	50	78.6	28.3	1532.91	0.0177934
258	Feng and Diao (2013)	29.8	2	0.1650	0.3300	200	500	7.8	184.4	0	60	78.6	28.3	1482.96	0.0147617
259	Feng and Diao (2013)	29.8	1	0.1650	0.4950	200	500	7.8	184.4	0	30	78.6	28.3	1430.99	0.0153045
260	Feng and Diao (2013)	29.8	1	0.1650	0.4950	200	500	7.8	184.4	0	60	78.6	28.3	1345.59	0.0150564

f'_c – Strength of unconfined concrete cylinder under compression (MPa); D – Diameter of PVC tube (mm); H – Height of concrete column (mm); t_p – Thickness of PVC tube (mm); D_c – Diameter of the concrete core without PVC tube (mm); e – Eccentricity distance (mm); P_{FP} – Peak finite element modeling load (kN); ϵ_{FP} – Peak finite element modeling strain (mm/mm)

Abbreviations

A_c	Cross-sectional area of concrete core (mm ²)
A_g	Gross-sectional area of concrete column (mm ²)
PVC	Polyvinyl chloride
CFPT	Concrete-filled PVC tube
CFRP	Carbon fiber reinforced polymer
CCFPT	Carbon fiber reinforced polymer concrete filled PVC tube
f_{cc}	Confined concrete compressive strength (MPa)
f_{co}	Unconfined concrete compressive strength (MPa)
t	Thickness of PVC tube (mm)
D	Diameter of PVC tube (mm)
L/H	Length/height of PVC tube (mm)
f_{cc}/f_{co}	Confined concrete compressive strength to unconfined concrete compressive strength Ratio
D_c	Diameter of concrete core without PVC tube (mm)
f_{I_c}	Strength of unconfined concrete cylinder under compression (MPa)
ε_{EP}	Peak experimental strain (mm/mm)
ε_{FP}	Peak finite element modeling strain (mm/mm)
P_{EP}	Peak experimental load (kN)
P_{FP}	Peak finite element modeling load (kN)
Ψ	Dilation angle
K_c	Shape factor for yielding surface
e_1	Plastic flow potential eccentricity
e	Eccentricity distance (mm)
μ	Viscosity parameter
f_{bo}/f'_{c}	Ratio of biaxial stress to uniaxial stress
f''_{c}	Considered to be 80% of concrete cylinder strength (MPa)
ε_{cc1}	Strain of confined concrete at first peak load (mm/mm)
ε_{co}	0.002 for unconfined concrete strength at peak load (mm/mm)
K_{es}	Ratio of effectively confined concrete area to confined area
f_yt	Yield strength of steel (MPa)
AAE	Average absolute error
MSE	Mean square error
MAE	Mean absolute error
RMSE	Root mean square error
VAF	Variance account factor
NS	Nash–Sutcliffe efficiency
RRSE	Root relative square error
RAE	Relative absolute error
KGE	Kling–Gupta efficiency
R^2	Coefficient of determination
f_l	Yield stress of longitudinal steel reinforcement (MPa)
f_h	Yield stress of hoop steel reinforcement (MPa)
f_{PVC}	Yield stress of PVC (MPa)
E_c	Young's modulus of concrete (MPa)
G	Shear modulus
μ	Poisson's ratio
MCR	Modified confined pressure ratio
ρ_{PVC}	Volumetric ratio of PVC tube
ρ_l	Volumetric ratio of longitudinal reinforcement
ρ_h	Volumetric ratio of longitudinal reinforcement
ρ_{CFRP}	Volumetric ratio of CFRP
f_{yl}	Yield strength of longitudinal reinforcement (MPa)
f_{yh}	Yield strength of hoop reinforcement (MPa)
f_{PVC}	Yield strength of PVC (MPa)
E_{CFRP}	Young's modulus of CFRP (MPa)
CDMP	Concrete damaged plasticity model
SR	Slenderness ratio
LCC	Load-carrying capacity
H	Height of concrete column (mm)
REC	Regression error characteristics
CDF	Cumulative distribution function
FEM	Finite element modeling
FRP	Fiber reinforced polymer

Acknowledgements

The authors extend their appreciation to King Saud University, Saudi Arabia, for funding this work through Researchers Supporting Project number (RSPD2024R704), King Saud University, Riyadh, Saudi Arabia.

Author contributions

Conceptualization, Project Administration, Funding, Supervision: H.F.I., and M.S.; Conceptualization, Formal Analysis, Methodology, Investigation, Validation, Writing – original draft: Y.W., A.Y.H., D.N.Q.; Visualization: Software, Data Curation, Resources: P.J., A., M.E.; Review & Editing: G.G.T., Y.W. All authors have read and agreed to the published version of the manuscript.

Availability of data and materials

All data are available with the corresponding author.

Declarations**Ethics approval and consent to participate**

None of experiments were performed on animals or human beings.

Competing interests

The authors declare no competing interests.

Received: 27 May 2024 Accepted: 14 December 2024

Published online: 17 February 2025

References

1. Zhao JL, Xu CH, Sun LZ, Wu DY. Behaviour of FRP-confined compound concrete–filled circular thin steel tubes under axial compression. *Adv Struct Eng.* 2020;23(9):1772–84. <https://doi.org/10.1177/1369433219900941>.
2. Hassanein MF, Hamed AY, Cashell KA, Shao YB. Confinement-based direct design of fibre reinforced polymer confined normal and high-strength CFST short columns. *Thin-walled Struct J.* 2023;192:111207. <https://doi.org/10.1016/j.tws.2023.111207>.
3. Jomaa'h MM, Salahaldin Al, Saber QA, Raheem AM. Large scale laboratory setup for testing structural performance of slender high-strength concrete columns subjected to axial load and fire: a preliminary study. In: Geotechnical Engineering and Sustainable Construction: Sustainable Geotechnical Engineering. Singapore: Springer Singapore. 2022. p. 611–626.
4. Isleem HF, Tahir M, Wang Z. Axial stress–strain model developed for rectangular RC columns confined with FRP wraps and anchors. *Structures.* 2020;23:779–88.
5. Isleem HF, Yusuf BO, Xingchong W, Qiong T, Jagadesh P, Augustino DS. Analytical and numerical investigation of polyvinyl chloride (PVC) confined concrete columns under different loading conditions. *Aust J Struct Eng.* 2024;25(1):69–97.
6. Yu F, Yin W, Cheng A, Vu QV, Wang S, Kong Z. Seismic behavior of PVC-CFRP confined reinforced concrete columns: an experimental study. *Structures.* 2021;32:313–28. <https://doi.org/10.1016/j.istruc.2021.03.003>.
7. Yu F, Xu G, Niu D, Cheng A, Wu P, Kong Z. Experimental study on PVC-CFRP confined concrete columns under low cyclic loading. *Constr Build Mater.* 2018;177:287–302. <https://doi.org/10.1016/j.conbuildmat.2018.05.111>.
8. Yue C, Isleem HF, Qader DN, Mahmoudian A, Weiming T, JANGIR P, Hamed AY. Utilization finite element and machine learning methods to investigation the axial compressive behavior of elliptical FRP-confined concrete columns. In: *Structures:* Elsevier. 2024, vo, 70, p. 107681. <https://doi.org/10.1016/j.istruc.2024.107681>.
9. Fakharifar M, Chen G. Compressive behavior of FRP-confined concrete-filled PVC tubular columns. *Compos Struct.* 2016;141:91–109.
10. Kassim MM, Ahmad SA. Strength evaluation of concrete columns with cross-sectional holes. *Pract Periodical Struct Design Constr.* 2018;23(4):04018027.
11. Feng Y, Diao N. Experimental study on PVC-CFRP confined reinforced concrete short column under axial compression. *J Build Struct.* 2013;34(6):129.
12. Jiang SF, Ma SL, Wu ZQ. Experimental study and theoretical analysis on slender concrete-filled CFRP–PVC tubular columns. *Constr Build Mater.* 2014;53:475–87.
13. Yu F, Cheng A, Xu G, Li D. Nonlinear finite element analysis of PVC-FRP confined concrete short column under axial compression. *Ind Constr.* 2015;45:77–82.
14. Yu F, Li D, Niu D. Analysis of bearing capacity of PVC-FRP confined concrete 789 column under eccentric compression. *J Xi'an Univ Archit Technol.* 2014;46:660–4.
15. Yu F, Li DA, Niu DT. A model for ultimate bearing capacity of PVC-CFRP confined concrete column with reinforced concrete beam joint under axial compression. *Constr Build Mater.* 2019;214:668–76. <https://doi.org/10.1016/j.conbuildmat.2019.04.131>.
16. Yu F, Zhang N, Niu D, Kong Z, Zhu D, Wang S, Fang Y, Yu F, Zhang NN, Niu DT, et al. Strain analysis of PVC-CFRP confined concrete column with ring beam joint under axial compression. *Compos Struct.* 2019;224:111012.
17. Yu F, Li Z, Fang Y, Zhu D, Kong Z. Mechanical behaviour of PVC-CFRP confined concrete column with RC beam joint subjected to axial load. *Gradévinar.* 2020;72(2):151–64.
18. Pan Y, Zhang L. Roles of artificial intelligence in construction engineering and management: a critical review and future trends. *Autom Constr.* 2021;122:103517.
19. Pham TM, Hadi MN. Predicting stress and strain of FRP-confined square/rectangular columns using artificial neural networks. *J Composite Constr.* 2014;18:04014019.
20. Wang C, Chan TM. Machine learning (ML) based models for predicting the ultimate strength of rectangular concrete-filled steel tube (CFST) columns undereccentric loading. *Eng Struct.* 2023;276:115392.

21. Zhou XG, Hou C, Feng WQ. Optimized data-driven machine learning models for axial strength prediction of rectangular CFST columns. *Structures*. 2023;47:760–80. <https://doi.org/10.1016/j.istruc.2022.11.030>.
22. Lyu F, Fan X, Ding F, Chen Z. Prediction of the axial compressive strength of circular concrete-filled steel tube columns using sine cosine algorithm-support vector regression. *Compos Struct*. 2021;273:114282. <https://doi.org/10.1016/j.compstruct.2021.114282>.
23. Isleem HF, Peng F, Tayea BA. Artificial Neural Network (ANN) and Finite Element (FE) models for simulating the axial compression behavior of GFRP RC columns. *Materials MDPI*. 2021. <https://doi.org/10.3390/ma14237172>.
24. Isleem HF, Tayeh BA, Abid MM, Iqbal M, Mohamed AM, El Sherbiny MG. Finite Element (FE) and Artificial Neural Network (ANN) modeling of FRP-RC columns under axial compression loading. *Front Mater Struct Mater*. 2022. <https://doi.org/10.3389/fmats.2022.888909>.
25. Isleem HF, Reddy Chukka ND, Bahrami A, Oyebisi S, Kumar R, Qiong T. Nonlinear finite element and analytical modeling of reinforced concrete filled steel tube columns under axial compression loading. *Results Eng*. 2023;19:101341. <https://doi.org/10.1016/j.rineng.2023.101341>.
26. Zarringol M, Thai HT, Naser MZ. Application of machine learning models for designing CFCFST columns. *J Constr Steel Res*. 2021;185:106856. <https://doi.org/10.1016/j.jcsr.2021.106856>.
27. Bardhan A, Biswas R, Kardani N, Iqbal M, Samui P, Singh MP, Asteris P. A novel integrated approach of augmented grey wolf optimizer and ANN for estimating axial load carrying-capacity of concrete-filled steel tube columns. *Constr Build Mater*. 2022;337:127454. <https://doi.org/10.1016/j.conbuildmat.2022.127454>.
28. Hou C, Zhou XG. Strength prediction of circular CFST columns through advanced machine learning methods. *J Build Eng*. 2022;51:104289. <https://doi.org/10.1016/j.jobe.2022.104289>.
29. Isleem HF. Confinement model for LRS FRP-confined concrete using conventional regression and artificial neural network techniques. *Compos Struct*. 2021;279:114779. <https://doi.org/10.1016/j.compstruct.2021.114779>.
30. Isleem HF, Qiong T, Reddy Chukka NK, Kumar R, Nagaraju TV, Hamed AY. Machine learning and nonlinear finite element analysis of fiber-reinforced polymer confined concrete-steel double-skin tubular columns under axial compression. *Struct Concr*. 2024. <https://doi.org/10.1002/suco.202300835>.
31. Xu C, Zhang Y, Isleem HF, Qiu D, Zhang Y, Alsaadawi MM, Tipu RK, El-Demerdash WE, Hamed AY. Numerical and machine learning models for concentrically and eccentrically loaded CFST columns confined with FRP wraps. *Struct Concr*. 2024. <https://doi.org/10.1002/suco.202400541>.
32. Fang Y, Yu F, Guan Y, Wang Z, Feng C, Li D. A model for predicting the stress-strain relation of PVC-CFRP confined concrete stub columns under axial compression. *Structures*. 2020;26:259–70.
33. Chang Y, Chen W, Xiao Q, Rong E, Peng L. Theoretical and experimental study on axial compression concrete-filled tubes with different confinements. *J Constr Steel Res*. 2021;185:106862.
34. Bandyopadhyay A, Samanta AK, Michel Paul K. Assessment of axial capacity of RC stub column confined with unplasticized polyvinyl chloride pipe. *J Inst Eng Vols Ser A*. 2019;100:535–46. <https://doi.org/10.1007/s40030-019-00397-5>.
35. Woldemariam AM, Oyawa WO, Nyomboi T. Structural performance of uPVC confined concrete equivalent cylinders under axial compression loads. *Buildings*. 2019;9(4):82.
36. Alatshan F, Altłomate A, Hamad S. Concrete filled plastic stub columns strength under axial compression. *Open J Civ Eng*. 2022;12(1):87–100.
37. Gupta PK, Verma VK. Study of concrete-filled unplasticized poly-vinyl chloride tubes in marine environment. *Proc Inst Mech Eng Part M Eng Marit Environ*. 2016;230(2):229–40.
38. Niu FYAD. Stress-strain model of PVC-FRP confined concrete column subjected to axial compression. *Int J Phys Sci*. 2010;5(15): 2304–2309.
39. Isleem HF, Jagadesh P, Qaidi S, Althoey F, Rahmawati C, Najm HM, Sabri MM. Finite element and theoretical investigations on PVC-CFRP confined concrete columns under axial compression. *Front Mater*. 2022;9:1055397. <https://doi.org/10.3389/fmats.2022.1055397>.
40. Isleem HF, Jagadesh P, Ahmad J, Qaidi S, Althoey F, Najm HM, Sabri MM. Finite element and analytical modelling of PVC-confined concrete columns under axial compression. *Frontiers in Materials*. 2022;9:1011675. <https://doi.org/10.3389/fmats.2022.1011675>.
41. ABAQUS Standard User's Manual. The Abaqus Software is a product of Dassault Systems Simulia Corp. Providence, RI, USA Dassault Systems, Vols. Version 6.13, USA, 2013.
42. Raza A, Ahmad A. Numerical investigation of load-carrying capacity of GFRP-reinforced rectangular concrete members using CDP model in ABAQUS. *Adv Civ Eng*. 2019. <https://doi.org/10.1155/2019/1745341>.
43. Isleem HF, et al. Finite element, analytical, artificial neural network models for carbon fibre reinforced polymer confined concrete filled steel columns with elliptical cross sections. *Front Mater*. 2023;9:1115394.
44. Xu Y, Tang H, Chen J, Jia Y, Liu R. Numerical analysis of CFRP-confined concrete-filled stainless steel tubular stub columns under axial compression. *J Build Eng*. 2021;37:102130.
45. Anand P, Sinha AK, Kumar C. Investigation of reinforced concrete jacketed columns under different loading conditions. *Int J Adv Technol Eng Explor*. 2021;8(81):957.
46. Tang H, Chen J, Fan L, Sun X, Peng C. Experimental investigation of FRP-confined concrete-filled stainless steel tube stub columns under axial compression. *Thin-Walled Struct*. 2020;146:106483.
47. Shao YB, Hamed AY, Elsisy AR, Nyarkod MH, Radu D, Hassanein MF. Confinement-based direct design of square normal and high strength steel tube confined concrete (STCC) short columns. *Structure*. 2024;65:106705. <https://doi.org/10.1016/j.istruc.2024.106705>.
48. Hassanein MF, Hamed AY, Shao YB, Silvest N. Confinement-based direct design of circular steel tube confined concrete (STCC) short columns. *J Constr Steel Res*. 2023;204:107871.
49. Hamed AY. Elastic shear buckling of tapered steel plate girders with opening in web. *J Eng Sci (JES)*. 2023;51(3):148–72. <https://doi.org/10.21608/JESAUN.2023.177464.1184>.
50. Hassan A, Arif M, Sharif M. Use of geopolymers concrete for a cleaner and sustainable environment—a review of mechanical properties and microstructure. *J Clean Prod*. 2019;223:704–28.
51. Building code requirements for structural concrete, United States: ACI, 2019.

52. Özkılıç YO, Aksöy C, Arslan MH. Numerical evaluation of effects of shear span, stirrup spacing and angle of stirrup on reinforced concrete beam behaviour. *Struct Eng Mech Int'l J.* 2021;79(3):309–26.
53. Youssf O, ElGawady MA, Mills JE, Ma X. Finite element modelling and dilation of FRP-confined concrete columns. *Eng Struct.* 2014;79:70–85.
54. Papanikolaou VK, Kappos AJ. Confinement-sensitive plasticity constitutive model for concrete in triaxial compression. *Int J Solids Struct.* 2007;44(21):7021–48.
55. Wu YF, Jiang C. Effect of load eccentricity on the stress-strain relationship of FRP-confined concrete columns. *Compos Struct.* 2013;98:228–41.
56. Hadi MN, Widarsa IR. Axial and flexural performance of square RC columns wrapped with CFRP under eccentric loading. *J Compos Constr.* 2012;16(6):640–9.
57. Abdulla NA. A strain model for uPVC tube-confined concrete. *Cogent Engineering.* 2021;8(8):1868695.
58. Wang JY, Yang QB. Investigation on compressive behaviors of thermoplastic pipe confined concrete. *Constr Build Mater.* 2012;35:578–85.
59. Hammadi AA, Khaleel F, Afan HA, Khan MH, Sulaibi AA. Study of behaviour of short concrete columns confined with PVC Tube under Uniaxial Load. *Appl Sci.* 2022;12(22):11427.
60. Ostrowski K, Dudek M, Sadowski Ł. Compressive behaviour of concrete-filled carbon fiber-reinforced polymer steel composite tube columns made of high performance concrete. *Compos Struct.* 2020;234:111668.
61. Wang Z, Wang D, Smith ST, Lu D. CFRP-confined square RC columns. I: experimental investigation. *J Compos Constr.* 2012;16(2):150–60.
62. Wang Z, Wang D, Smith ST. Experimental testing and analytical modeling of CFRP-confined large circular RC columns subjected to cyclic axial compression. *Eng Struct.* 2012;40:64–74.
63. Bassi A, Mir AA, Kumar B, Patel M. A comprehensive study of various regressions and deep learning approaches for the prediction of friction factor in mobile bed channels. *J Hydroinf.* 2023;25(6):2500–21.
64. Deng Z, Zhu X, Cheng D, Zong M, Zhang S. Efficient kNN classification algorithm for big data. *Neurocomputing.* 2016;195:143–8.
65. Zhang ML, Zhou ZH. ML-KNN: A lazy learning approach to multi-label learning. *Pattern Recogn.* 2007;40(7):2038–48.
66. Lu D, Wang G, Du X, Wang Y. A nonlinear dynamic uniaxial strength criterion that considers the ultimate dynamic strength of concrete. *Int J Impact Eng.* 2017;103:124–37. <https://doi.org/10.1016/j.ijimpeng.2017>.
67. Singh R, Patel M. Experimental and machine learning approaches to investigate the application of sugarcane bagasse ash as a partial replacement of fine aggregate for concrete production. *J Build Eng.* 2023;76:107168.
68. Wadhawan S, Bassi A, Singh R, Patel M. Prediction of compressive strength for fly ash-based concrete: critical comparison of machine learning algorithms. *J Soft Comput Civ Eng.* 2023;7(3):68–110.
69. Wei J, Ying H, Yang Y, Zhang W, Yuan H, Zhou J. Seismic performance of concrete-filled steel tubular composite columns with ultra high performance concrete plates. *Eng Struct.* 2023;278:115500. <https://doi.org/10.1016/j.engstruct.2022.115500>.
70. Song X, Wang W, Deng Y, Su Y, Jia F, Zaheer Q, Long X. Data-driven modeling for residual velocity of projectile penetrating reinforced concrete slabs. *Eng Struct.* 2024;306:117761. <https://doi.org/10.1016/j.engstruct>.
71. Bassi A, Manchanda A, Singh R, Patel M. A comparative study of machine learning algorithms for the prediction of compressive strength of rice husk ash-based concrete. *Nat Hazards.* 2023. <https://doi.org/10.1007/s11069-023-05998-9>.
72. Kavitha S, Varuna S, Ramya R. A comparative analysis on linear regression and support vector regression," online international conference on green engineering and technologies (IC-GET). IEEE, 1–5, 2016.
73. Yao W, Li L. A new regression model: modal linear regression. *Scand J Stat.* 2014;41(3):656–71.
74. Xu DS, Yan JM, Liu Q. Behavior of discrete fiber-reinforced sandy soil in large-scale simple shear tests. *Geosynth Int.* 2021;28(6):598–608. <https://doi.org/10.1680/jgein.21.00007>.
75. He L, Pan J, Hee YS, Chen H, Li LG, Panda B, Chow WT. Development of novel concave and convex trowels for higher interlayer strength of 3D printed cement paste. *Case Stud Constr Mater.* 2024;21:e03745. <https://doi.org/10.1016/j.cscm.2024.e03745>.
76. Mosavi A, Sajedi Hosseini F, Choubin B, Goodarzi M, Dineva AA, Rafiee Sardooi E. Ensemble boosting and bagging based machine learning models for groundwater potential prediction. *Water Resour Manag.* 2021;35:23–37.
77. Shahani NM, Kamran M, Zheng X, Liu C, Guo X. Application of gradient boosting machine learning algorithms to predict uniaxial compressive strength of soft sedimentary rocks at Thar Coalfield. *Adv Civ Eng.* 2021. <https://doi.org/10.1155/2021/2565488>.
78. Huang H, Guo M, Zhang W, Zeng J, Yang K, Bai H. Numerical investigation on the bearing capacity of RC columns strengthened by HPFL-BSP under combined loadings. *J Build Eng.* 2021;39:102266.
79. Guo M, Huang H, Zhang W, Xue C, Huang M. Assessment of RC frame capacity subjected to a loss of corner column. *J Struct Eng.* 2022. [https://doi.org/10.1061/\(ASCE\)ST.1943-541X.0003423](https://doi.org/10.1061/(ASCE)ST.1943-541X.0003423).
80. Cutler DR, Edwards TC Jr, Beard KH, Cutler A, Hess KT, Gibson J, Lawler JJ. Random forests for classification in ecology. *Ecology.* 2007;88(11):2783–92.
81. Qi Y. Random forest for bioinformatics. In: Zhang C, Ma Y, editors. *Ensemble machine learning: Methods and applications.* New York: Springer; 2012. p. 307–23.
82. Fawagreh K, Gaber MM, Elyan E. Random forests: from early developments to recent advancements. *Syst Sci Control Eng Open Access J.* 2014;2(1):602–9.
83. Huang H, Xue C, Zhang W, Guo M. Torsion design of CFRP-CFST columns using a data-driven optimization approach. *Eng Struct.* 2022;251:113479. <https://doi.org/10.1016/j.engstruct.2021.113479>.
84. Zhang J, Zhang C. Using viscoelastic materials to mitigate earthquake-induced pounding between adjacent frames with unequal height considering soil-structure interactions. *Soil Dyn Earthq Eng.* 2023;172:107988. <https://doi.org/10.1016/j.soildyn.2023.107988>.
85. Zhang C, Duan C, Sun L. Inter-storey isolation versus base isolation using friction pendulum systems. *Int J Struct Stab Dyn.* 2024;24(2):2450022. <https://doi.org/10.1142/S0219455424500226>.

86. Chen R, Zhao B, Xin Q, Niu X, Xie Z, Lu X, Zou D. Analysis of transient lubrication and wear coupling behaviors considering thermal effect and journal misalignment for main bearings under dynamic load. *Wear.* 2024. <https://doi.org/10.1016/j.wear.2024.205478>.
87. Zhang C, Shu J, Zhang H, Ning Y, Yu Y. Estimation of load-carrying capacity of cracked RC beams using 3D digital twin model integrated with point clouds and images. *Eng Struct.* 2024;310:118126.
88. Wang J, Han J, Zhu C, Lu W, Zhang Y, He X, Chen Y. Structural optimization and engineering application of concrete-filled steel tubular composite supports. *Eng Fail Anal.* 2024;159:108082. <https://doi.org/10.1016/j.Engstruct.2024.118126>.
89. Diao X, Song Y, Pan S, Cai X, Shi T, Wang L. Enhanced dynamic compressive performance of silicon carbide whiskers-modified mortars. *Constr Build Mater.* 2024;432:136626. <https://doi.org/10.1016/j.conbuildmat.2024.136626>.
90. Wang Z, Wang K, Han Q, Ni J, Wu Z. Crack imaging of underwater concrete components using interfacial waves and transducer array. *Mech Syst Signal Process.* 2025;224:111998. <https://doi.org/10.1016/j.jmssp.2024.111998>.

Publisher's Note

Springer Nature remains neutral with regard to jurisdictional claims in published maps and institutional affiliations.